Hydrodynamic performance of a floating breakwater as an oscillating-buoy type wave energy converter

Hengming Zhang[a], Binzhen Zhou[a, b*], Christopher Vogel[b], Richard Willden[b], Jun Zang[c], Liang Zhang[a]

[a]*College of Shipbuilding Engineering, Harbin Engineering University, Harbin 150001, China*
[b]*Department of Engineering Science, University of Oxford, OX1 3PJ, United Kingdom*
[c]*Department of Architecture and Civil Engineering, University of Bath, Bath, BA2 7AY, UK*

Abstract

Combined floating breakwater and wave energy converter systems have the potential to provide a cost-effective solution to offshore power supply and coastal protection. This will make wave energy economically competitive and commercial-scale wave power operations possible. This paper investigates the hydrodynamic features of wave energy converters that meet the dual objectives of wave energy extraction and attenuation for such a combined system. A two-dimensional numerical model was established using Star-CCM+ commercial software based on viscous Computational Fluid Dynamics theory to investigate the hydrodynamic performance of an oscillating buoy Wave Energy Converter (WEC) type floating breakwater under regular waves. The model proposed in this paper was verified with published experimental results. The hydrodynamics of symmetric and asymmetric floaters were investigated to demonstrate their wave attenuation and energy extraction performance, including square bottomed, triangular bottomed (with and without a baffle plate), and the Berkley Wedge. The asymmetric floaters were found to have higher power conversion efficiency and better wave attenuation performance, especially the Berkeley Wedge bottom device and the triangular-baffle bottom device. The triangular-baffle bottom device with a simpler geometry achieved similar wave attenuation and energy extraction performance characteristics to that of the Berkeley Wedge device. The maximum energy conversion efficiency of the triangular-baffle bottom floater reached up to 93%, an impressive WEC device among many designs for wave energy conversion. There may be a great potential for this newly proposed triangular-baffle bottom WEC type of floater to be an ideal coastal structure for both coastal protection and wave energy extraction.

Key Word: Floating breakwaters; Wave energy converter; Integrated system; Wave attenuation; Wave energy extraction

* Corresponding author
E-mail address: zhoubinzhen@hrbeu.edu.cn (B.Z. Zhou)

1. Introduction

Wave energy is one of the most promising ocean renewable energy resources because of its high energy density, predictability, and wide-spread availability [1]. However, the capital costs of Wave Energy Converters (WECs) currently exceed those of conventional generation technologies (e.g., gas, coal) and other renewable energies (e.g. solar photovoltaics, wind energy) [2], which have made the electricity generated by WECs less competitive. Integration of WECs and floating breakwaters has been proposed as one way of helping to reduce costs, which has been introduced by Mustapa et al. [3] and Zhao et al. [4].

Floating breakwaters are widely used in port engineering, artificial beaches, and marine aquaculture. Key advantages of floating breakwaters are the reduced requirements on seabed conditions, low environmental impact and flexibility compared to seabed mounted breakwaters, for which cost is a strong function of water depth [5]. Most floating breakwaters attenuate ocean waves by reflecting incoming waves [6]. In practice, breakwater width usually needs to be at least one-third of the target wave length for satisfactory wave attenuation, which makes the construction cost high when designing for long waves [7]. WECs installed on floating breakwaters can usefully extract part of the wave energy rather than simply dissipating energy, which has the benefits of both cost-sharing and providing offshore power supply and may improve project economics [1]. Co-installation may also help to reduce the impact forces acting on the breakwater, improving the lift span of the device and allowing it to work in heavier wave conditions. The wave attenuation performance of the integrated system may therefore exceed that of the stand-alone breakwater. The motivation of this study is to investigate the hydrodynamic features of WECs that meet the dual objectives of power production and wave attenuation for combined WEC-breakwater systems.

Various WEC concepts have been proposed for integration with breakwaters, including Oscillating Water Columns (OWC), overtopping and piston types. He et al. [8] experimentally studied the oscillating air-pressures inside the two chambers of an OWC-type converter integrated with a slack-moored floating breakwater, and the wave power extraction was investigated by He et al. [9]. He et al. [10] investigated the hydrodynamics of a pile-supported OWC breakwater based on linear wave theory and matched eigenfunction expansion method. Xu et al. [11] studied the hydrodynamic performance of a dual-functional wave-power plant based on the concept of integrating OWC devices into a pile breakwater through a series of wave flume tests. Zheng et al. [12] studied the performance of an OWC device integrated into a vertical structure in finite water depth using a novel theoretical model based on the linear potential flow. Giacomo et al. [13] introduced a theoretical and experimental study of a breakwater-integrated U-OWC wave energy converter with dielectric elastomer generator. All

of these studies show that the power production and wave attenuation performance of the integrated OWC devices is improved. Contestabile et al. [14] investigated an overtopping type WEC, and the nature and magnitude of wave loadings on various parts of the structure were analyzed. Yueh & Chuang [15] investigated the performance of a partially piston-type porous WEC that doubles as a wave-trapping maker.

Most of the proposed breakwaters were stationary, rather than floating. Floating breakwaters with simple rectangular cross-sections integrated with WECs have been investigated, generally through experiments. The hydrodynamic performance of a vertical pile-restrained WEC-type floating breakwater was experimentally investigated by Ning et al. [16]. Zhao & Ning [17] and Zhao et al. [18] demonstrated that the energy conversion efficiency of the single pontoon breakwater-type WEC system of Ning et al. [16] could be improved using a novel system consisting of a front oscillating buoy type WEC and a rear fixed pontoon. Potential flow theory is often used to develop an initial understanding of the hydrodynamic fundamentals of the integrated system. Zhao et al. [19] and Ning et al. [20] developed analytical models of a single and dual pontoon WEC-type floating breakwaters to study wave energy extraction and wave attenuation performance, respectively. However, linear potential theory can overestimate the motion and power response, especially around the resonance frequency of WECs [21], as viscous effects are neglected. An alternative approach is to use Computational Fluid Dynamics (CFD) methods, which can deal with strongly nonlinear phenomena such as vortex shedding and turbulence. Chen et al. [22] presented a numerical study on the hydrodynamic performance of a vertical pile-restrained WEC-type floating breakwater using a particle-in-cell method which has the potential to become a high-quality CFD tool, and an optimization study based on the numerical model was conducted focusing on modifying the shape of the floating breakwater. These studies focused on symmetric devices, whose performance meets the objectives for operation as both a WEC and breakwater.

Floater shape has a pronounced effect on the wave energy capture and attenuation performance, and hence is an important design question for a combined WEC-floating breakwater system. Symmetric heaving devices yield only 50% energy-capturing efficiency [20], whereas the Berkeley Wedge, an asymmetric heaving device proposed by Yeung et al. [23], improved the energy-capturing efficiency to 96.34% and the transmission coefficient was also improved significantly compared with the square bottom [24]. Zhang et al. [25] utilized a semi-analytical method based on the boundary discretization method to investigate the hydrodynamic and shape optimization for vertical axisymmetric wave energy converters, and showed that parabolic and conical absorbers were better at converting wave energy than

cylindrical absorbers in a random wave sea. The importance of device hydrodynamics was demonstrated by Chen et al. [26], who found that floaters with conical bottoms greatly improved WEC energy efficiency due to the smaller viscous damping compared with the square bottom. Reabroy et al. [27] numerically and experimentally investigated the hydrodynamic and power performance of an asymmetric WEC integrated with a fixed breakwater, and showed that the maximum power efficiency of the WEC model was 37.6%.

A combined WEC-floating breakwater system needs to have good wave attenuation and energy extraction characteristics, which helps make wave energy economically competitive. The dynamics of symmetric and asymmetric floaters are investigated, with particular focus on the wave attenuation and energy extraction features required for a combined floating breakwater and WEC system. A two-dimensional numerical model of wave interaction with the floating structure is developed using the finite volume CFD software Star-CCM+ due to its advantages as a well-developed software package with many modules for wave modelling and automatic meshing and powerful post processing capabilities. The accuracy of the numerical model is verified through comparison with the published experimental results of Ning et al. [20] and linear analytical results of Zhao et al. [19] with box-type bottom, and also published experimental results by Madhi et al. [24] for the Berkley-Wedge bottom. The optimal damping coefficients based on potential flow theory are consistent with the CFD results, and are then used for all cases. The wave energy conversion efficiency and the transmission coefficient of the device with different bottom shapes are compared. The effect of floater width, ratio of triangular wedge geometry and the height on integrated system performance is also investigated. The present results can provide a valuable guidance for the practical engineering design, manufacture and optimization of WEC-breakwater integrated devices.

2. Numerical model

In order to investigate the fluid/wave dynamics of what leads to improved wave attenuation and energy extraction performance, one symmetric floater with a square bottom and three asymmetric floaters with different bottom shapes are considered, including Triangular bottom, Berkeley-Wedge, and Triangular-baffle bottoms, as shown in Fig. 1.

2.1 Flow field model

A two-dimensional numerical wave tank for an incompressible viscous fluid was employed using Star-CCM+ CFD software. The governing Navier-Stokes equations are spatially discretized using the finite volume method, and the Volume of Fluid (VOF) method was applied to capture the free surface interface between the air and water phases [28]. The large

eddy simulation (LES) turbulence model was selected, with comparison made to the laminar flow model to evaluate the effect of turbulence in Section 3.2. In this paper, the length of the calculation domain in the x direction was taken to be six times the wavelength λ, and the height in the z direction was taken to be two times the water depth h, as shown in Fig. 2 (a), where the red and blue parts indicate the water and the air, respectively. The density of water is 10^3 kg/m^3 and the density of air is 0. Since a purely two-dimensional planar model cannot be simulated with the Star-CCM+ software, the width of the model L_y in the y direction was set to 0.01m and symmetry conditions on the front and back boundaries were used to ensure the two-dimensionality of the model [29], as shown in Fig. 2 (b), which is enlarged for the view.

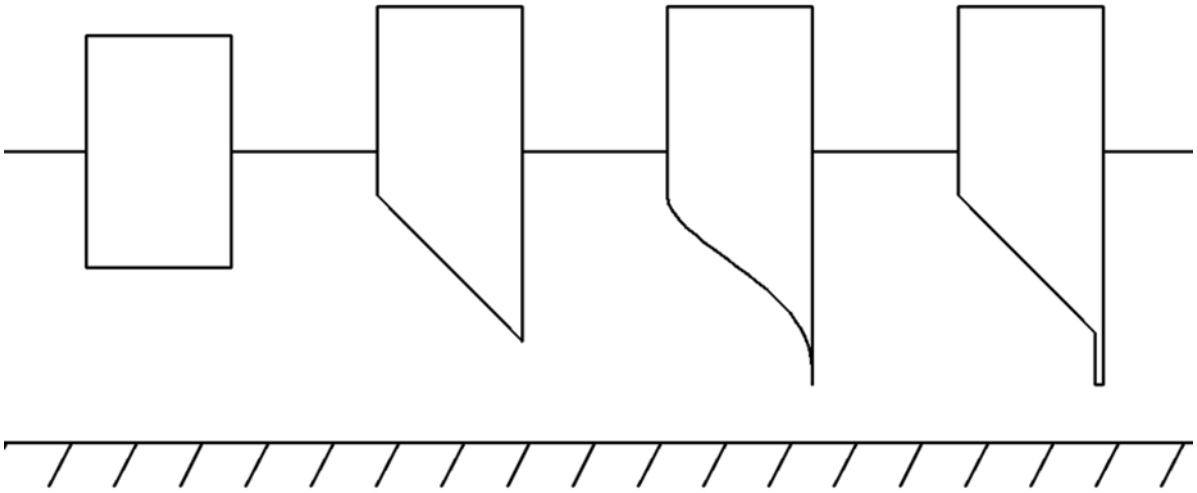

(a) Square bottom (b) Triangular bottom (c) Berkeley-Wedge bottom (d) Triangular-baffle bottom

Fig. 1 Schematic diagram of four floaters with different bottom shapes.

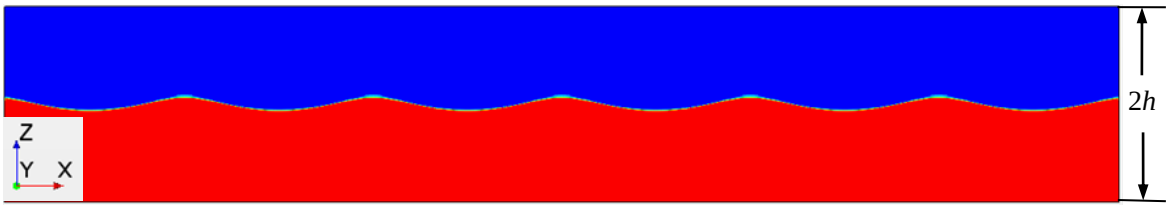

(a) Side view.

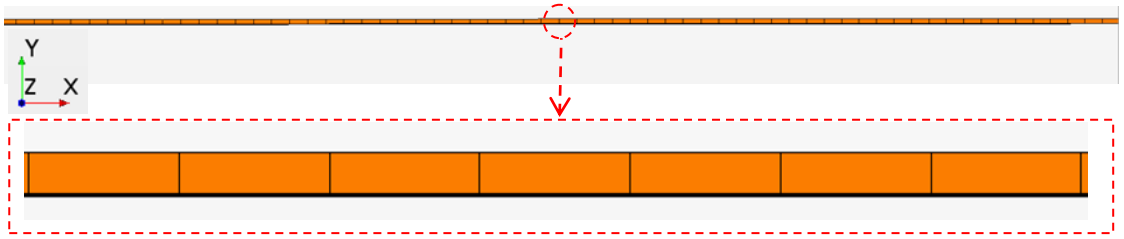

(b) Plan view.

Fig. 2 Side (a) and plan (b) views of the numerical wave tank model.

2.2 Mesh and boundary conditions

2.2.1 Boundary conditions

The boundaries of the model are shown in Fig. 3.

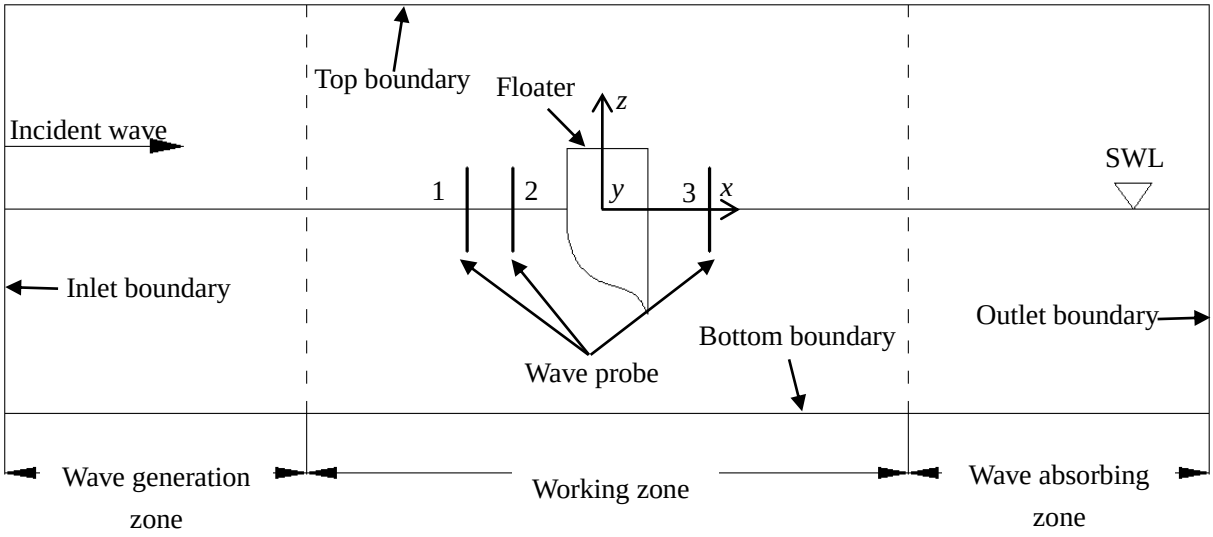

Fig. 3 A diagram of wave interaction with a floating body.

The inlet boundary was defined to be a velocity inlet. The inlet face velocity vector was specified as the velocity of a fifth-order VOF wave [30] directly and the working fluid was set to be two-phase flow of water and air. The horizontal (U) and vertical (W) velocities of the fifth-order VOF wave are given by

$$\begin{aligned} U &= \frac{\partial \Phi}{\partial X} \\ W &= \frac{\partial \Phi}{\partial Z} \end{aligned} \tag{1}$$

where X is the horizontal co-ordinate and Z is the vertical co-ordinate in a Cartesian coordinate system, Φ is the velocity potential given by

$$\Phi(X,Z,t) = (c-\bar{u})X + C_0\left(\frac{g}{k^3}\right)^{1/2}\sum_{i=1}^{5}\varepsilon^i\sum_{j=1}^{i}A_{ij}\cosh jkZ\sin jk(X-ct) \tag{2}$$

$$\bar{u}\left(\frac{k}{g}\right)^{1/2} = 1+\frac{1}{2}\varepsilon^2+\frac{1}{8}\varepsilon^4+\mathrm{O}(\varepsilon^6) \tag{3}$$

where c is the wave propagation velocity, C_0 and A_{ij} are model coefficients, which can be found in [30], k is the wave number, $\varepsilon=kH/2$ is the dimensionless wave amplitude, and g is gravitational acceleration.

Two different wave absorbing methods were evaluated for the outlet boundary. The

Forcing wave absorbing method showed better performance than the Damping method as shown in Fig. 4, comparing the heave motion of a H_i=0.2m at T=1.37s, where the floater width was 0.8m and the draft was 0.2m. The Forcing method showed more steady results than the Damping method, especially after t>10T. This is because the Forcing method can be applied both in the wave generation zone and the wave absorbing zone. Using the Forcing method allows to only keep the incident waves in these two zones, while all the other waves including reflected waves and scattered waves are absorbed, which helps improve the accuracy of long simulations. The Damping method only can be used in the wave absorbing zone since the incoming waves would be damped as well if it was applied in the wave generation zone. In Star-CCM+ software, the Forcing method is available for velocity inlet, pressure outlet, and symmetry boundaries. As a symmetry boundary is not appropriate at the outlet, the velocity inlet and pressure outlet boundary conditions were compared for the case with T=1.37s, H_i=0.2m, as shown in Fig. 5. The wave elevation is steady for both boundaries for t<18T; however, becomes unstable with the pressure outlet boundary at later times. Therefore, the outlet boundary was also defined to be the velocity inlet, and the outlet face velocity vector was specified as the velocity of a fifth-order VOF wave [30] as well.

A pressure outlet was assigned to the top boundary, where the pressure was specified as hydrostatic pressure of the fifth-order VOF wave and the composition of fluid components was air. A wall boundary condition was assigned to the bottom boundary to simulate the bottom condition of the tank. A subtracted area was introduced when a floater was placed in the tank. No-slip boundary conditions were assigned to the body surface. An overset mesh condition was assigned to the outer four surfaces.

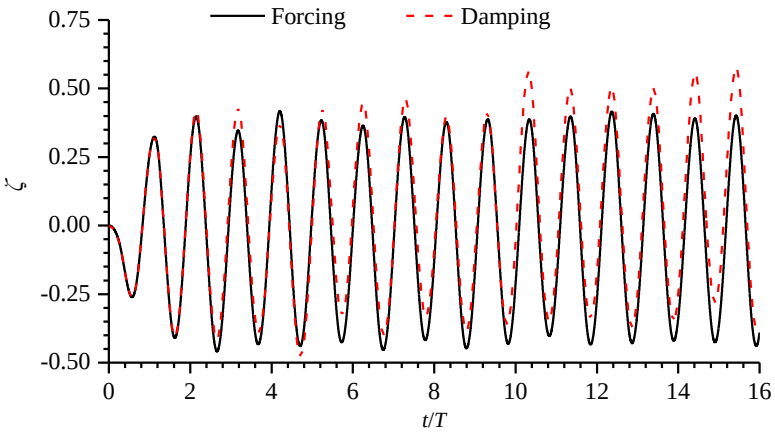

Fig. 4 Comparison of heave motion of a floating square box with different wave absorbing methods with T=1.37s, H_i=0.2m

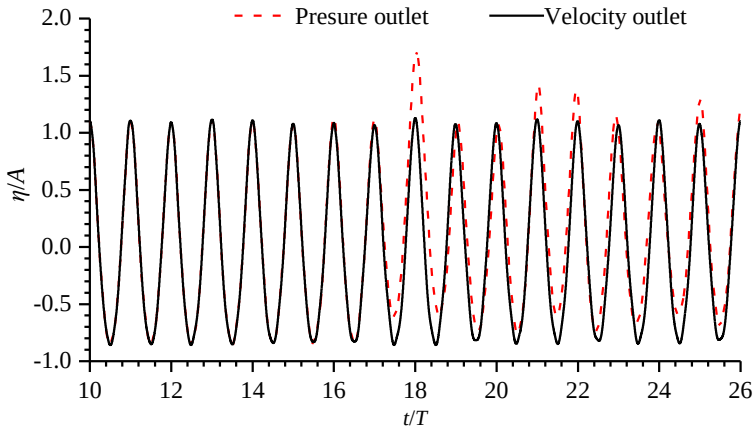

Fig. 5 Comparison of wave elevations at the centre of wave flume for models with different outlet boundary conditions with T=1.37s, H_i=0.2m.

2.2.2 Mesh generation technology

A trimmed cell mesher was selected to generate the meshes of the liquid level encryption zone, the liquid surface transition zone and the motion encryption zone. The Star CCM+ Trimmer Mesher generates hexahedral meshes that accommodate arbitrary geometry, and provides good quality meshes that have low computational cost. The surface remesher and the prism layer mesher were selected to generate a prismatic layer [31], which was chosen as ten layers, around the body surface, as shown in Fig. 6, where the water depth h=2.0m, the width of the body B/h=0.25, and the total draft D/h=0.4.

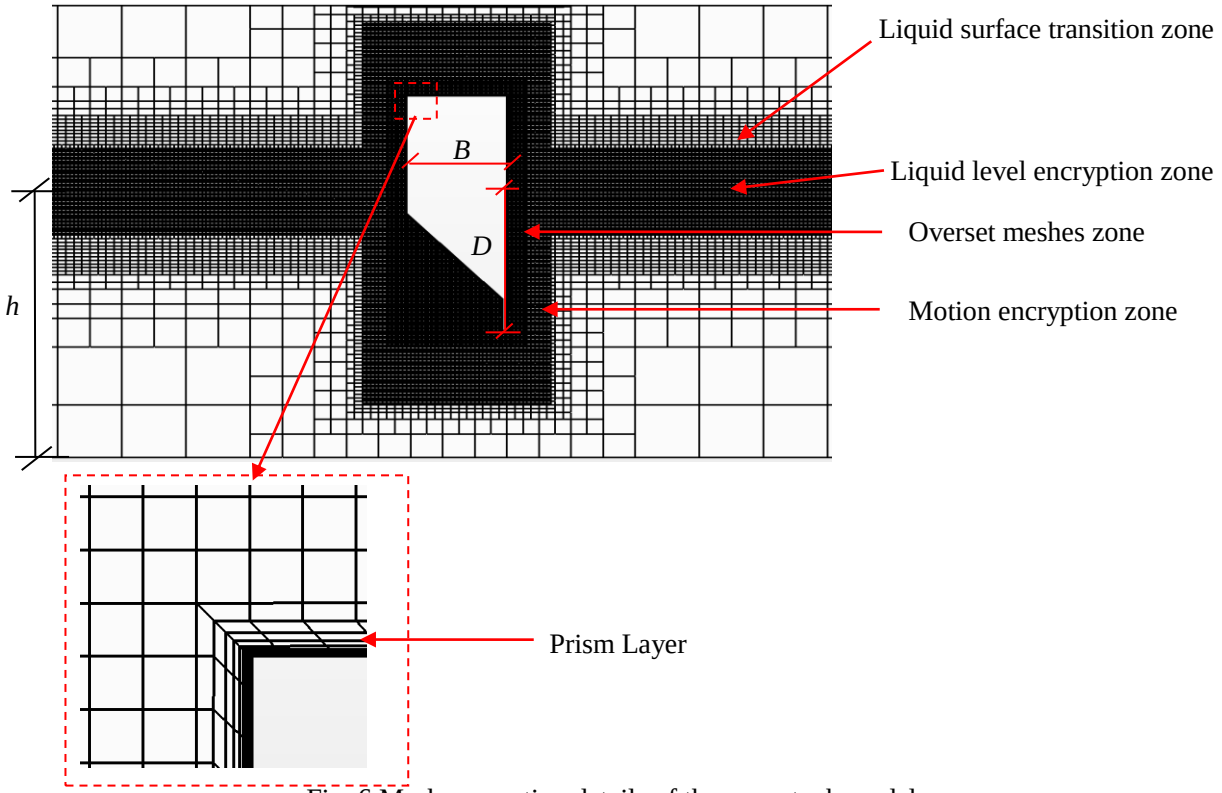

Fig. 6 Mesh generation details of the wave tank model.

An overset mesh zone was applied in order to divide the complex air-water interface region into simpler sub-domains. The flow in each sub-domain is calculated independently, and may overlap with each other. Matching and coupling at the intersection of the two domains are performed by interpolation, which is based on the dynamic distinction of different cell types. The cells can be active (solve), inactive (ignore) or dependent (interpolate) [32]. The overset mesh approach has been used widely in CFD codes such as Star CCM+ and PEGASUS, because the meshing approach offers improved accuracy in comparison to dynamic meshes for large-scale deformations.

2.3 Motion and energy conversion of floater

The floater, as shown in Fig. 3, was constrained to have heave motion only, and the equation of motion can be written as

$$m\ddot{z}+b_{\mathrm{pto}}\dot{z}+c_{\mathrm{pto}}z=-mg+F_{\mathrm{w}} \tag{4}$$

where m is the mass of the floater; z, $\dot{z}$ and $\ddot{z}$ are the heave motion, velocity and acceleration of the floater, respectively; b_{pto} and c_{pto} are the mechanical damping and elastic stiffness due to power take-off (PTO) system, respectively; F_{w} is the wave force, including buoyancy, in still water.

The resonance frequency is defined as the natural frequency of the object when the inertial force and the restoring force are in equilibrium [33], that is

$$\omega_{\mathrm{n}}=\sqrt{\frac{c_{\mathrm{pto}}+c_{\mathrm{z}}}{m+a_{\mathrm{z}}}} \tag{5}$$

For a single body with only a single mode of motion, the optimal PTO damping coefficient b_{opt} under wave frequency ω can be written as [33]

$$b_{\mathrm{opt}}=\sqrt{\frac{((m+a_{\mathrm{z}})\omega^2-(c_{\mathrm{pto}}+c_{\mathrm{z}}))^2}{\omega^2}+b_{\mathrm{z}}^2} \tag{6}$$

where a_{z} and b_{z} are the linear added mass and radiation damping coefficients of the floater, which are both functions of wave frequency, which are calculated through a two-dimensional numerical wave tank model based on potential flow theory [34][35]. $c_{\mathrm{z}}=\rho g A_{\mathrm{w}}$ is the restoring force coefficient due to the difference in the contributions from the hydrostatic term and the weight of the floater, in which A_{w} is the wetted surface of the floater.

The conversion efficiency η_{e} is an important indicator to evaluate the hydrodynamic efficiency of WECs [36], which can be expressed as

$$\eta_{\mathrm{e}}=E_{\mathrm{p}}/E_{\mathrm{w}} \tag{7}$$

where the average wave energy conversion power and the incident wave power can be calculated as:

$$E_{\mathrm{P}} = \frac{b_{\mathrm{pto}}}{nT} \int_{t}^{t+nT} V^2 \mathrm{d}t \tag{8}$$

$$E_{\mathrm{w}} = \frac{1}{16} \frac{\rho g H_{\mathrm{i}}^{\ 2} \omega D_y}{k} (1 + \frac{2kh}{\sinh 2kh}) \tag{9}$$

where H_{i} is the incident wave height, h is the water depth, V is the velocity of the floater, T is the wave period, D_y is the transverse length of floating breakwater, and n is the number of the floater motion period.

The wave transmission characteristic is an important factor for the functional role of a breakwater given the objective of wave protection, so the transmission coefficient K_{t} is introduced as

$$K_{\mathrm{t}} = \frac{H_{\mathrm{t}}}{H_{\mathrm{i}}} \tag{10}$$

where H_{t} is the transmission wave height obtained by a monitoring point set at x=0.8m behind the breakwater. The motion response ζ is defined as the ratio of floater motion amplitude H_{RAO} to the incident wave height H_{i}

$$\zeta = \frac{H_{\mathrm{RAO}}}{H_{\mathrm{i}}} \tag{11}$$

The dissipation coefficient K_{d} including the contribution from the energy loss in vortex shedding at floater corners is defined as

$$K_{\mathrm{d}} = 1 - K_{\mathrm{t}}^2 - K_{\mathrm{r}}^2 - \eta_{\mathrm{e}} \tag{12}$$

where K_{r} is the reflection coefficient defined as the ratio of reflection wave height H_{r} to the incident wave height H_{i}, that is

$$K_{\mathrm{r}} = \frac{H_{\mathrm{r}}}{H_{\mathrm{i}}} \tag{13}$$

which is obtained by a two-point method [37]. Two monitoring points of wave height which are used in two-point method are set at x=-1.6m and x=-2.4m in front of the breakwater.

3. Convergence study and verification

3.1 Convergence study

Propagation of regular waves without a floating body was simulated in the numerical wave tank (NWT) to verify the stability and accuracy of the model. Verification is necessary

because wave elevation generally decays along the wave flume due to viscosity, which is not modeled in potential theory. Model parameters with the wave period T=1.37s, the incident wave height H_i=0.2m and the water depth h=1m were considered. The length of the tank was defined as $L_x=6\lambda$, which was verified to be sufficiently long to minimize tank length effects. The left and right ends of the NWT were set as wave generation and wave absorbing zones respectively, which were both taken as 1.5λ. The laminar flow is not appropriate for some cases due to influence of eddies around the body, therefore, the choice of turbulence model was also investigated. The SST k-ω and k-ε are common RANS turbulence models, and comparison is also made to large eddy simulation (LES) which is generally more accurate than the RANS turbulence models [38]. LES can agree well with experiment data [39] [40], but require longer computation time than the RANS turbulence models. Fig. 7 shows the corresponding wave elevations at the centre of the wave flume with T=1.37s, H_i=0.2m using the different turbulence models. The wave elevations calculated by the k-ε and SST k-ω turbulence models begin to attenuate from t >14T and t >12T respectively, which happens for all mesh resolutions and time steps due to the dissipative ness of the models. Therefore, the laminar flow and the LES turbulence models were adopted in the present paper.

Five models (Model 1, Model 2, Model 3, Model 4 and Model 5) with three different meshes and three different time steps were investigated, with details of the meshes and time steps shown in Table 1. The corresponding wave elevations at the centre of the wave flume are shown in Fig. 8 (a) and Fig. 8 (b), and the higher order analytical solution obtained by stream function theory [41] is also given for comparison, where $A=H_i/2$ is the wave amplitude. Model 2 and Model 4 are almost identical and also agree well with the analytical solution, while the Model 5 is a little different from the analytical solution in troughs and peaks. Model

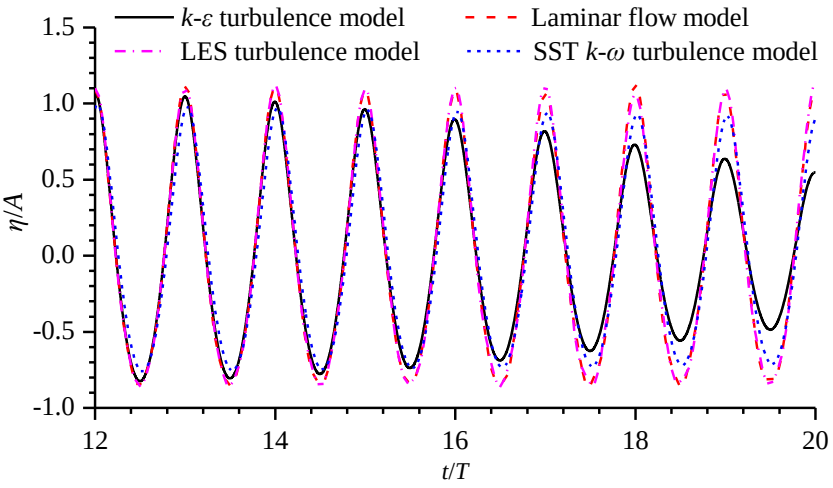

Fig. 7 Comparison of wave elevations at the centre of wave flume for different models with T=1.37s, H_i=0.2m.

1 with time step $\Delta t=T/500$ is a little different from the analytical solution in troughs, while the other two models agree well with the analytical solution. Thus it was concluded that Model 2 with mesh $\Delta z=H/20$, $\Delta x=2\Delta z$ in the liquid level encryption zone and time step $\Delta t=T/1000$ is sufficiently accurate. The spatial distribution of wave heights is presented in Fig. 8 (c). It can be seen that wave heights at both ends of the wave flume are close to the given wave height because only scattered waves are dissipated at both the left and right ends of the wave flume and the total velocity potential is forced to equal to the incident velocity potential. In the middle of the wave flume, the maximum attenuation of wave heights is about 3.5%, which provides sufficient accuracy for the applications considered herein.

A floating square box with the width B/h=0.8 and the draught D/h=0.2 was simulated in the middle of wave flume and restricted to heave motion only without the PTO damping, following one of the experimental cases of Ning et al. [20]. Fig. 9 shows the comparison of heave motions with three time steps (Model A, Model B and Model C) and three different meshes (Model B, Model D and Model E), as shown in Table 2. From Fig. 9 (a), it can be seen that, for Model B and Model C, only slight differences are observed in peaks and troughs, with the error being less than 5%, while the result of Model A is obviously different from the other two models. It can be seen in Fig. 9 (b) that Model D does not match well with the results of Model B and Model E. Therefore, Model B with mesh $\Delta z=H/20$, $\Delta x=2\Delta z$ in the motion encryption zone and time step $\Delta t=T/1000$ is considered to be sufficiently accurate for modelling a floating body.

The value of $y+$ in turbulence modelling is very important, and needs to be evaluated to determine the convergence of LES turbulence model. A “Berkeley-Wedge” floater [24] with three different values of $y+$ (Model a, Model b and Model c) is investigated under the optimal PTO damping. The width of the “Berkeley- Wedge” floater was B/h=0.33 and the draught was D/h=0.53. The value of $y+$ is related to the thickness of the prism layer and the number of layers near boundaries, as shown in Table 3. Fig. 10 shows the comparison of heave motion of the “Berkeley-Wedge” floater with different $y+$ with H_i=0.0508m at T=1.556s. The results of three models with different value of $y+$ are nearly the same for $t/T<14$. However, Model c diverges from the other cases when $t/T>14$, whereas Models a and b still match well. Therefore, it was concluded that the $0.01<y+<0.8$ of Model b is small enough to get convergent results. For other cases in this paper, the value of $y+$ for LES turbulence model remained within 0.01-0.8.

The length of the tank $L_x=6\lambda$ was verified to be long enough through comparison to other tank lengths. Fig. 11 (a) shows the comparison of heave motion ζ of floating square box models with different lengths of tank, where the wave height H_i=0.2m, the wave period

T=1.37s and the wave generation zone and wave absorbing zone were 1.5λ. It can be seen that three results are almost identical as t<10T. However, the result with L_x=4λ is different from the other results with L_x=6λ and L_x=9λ. Therefore, L_x=6λ is long enough to simulate this case. The width of the tank L_y=0.01m was also verified to be accurate enough to simulate the interaction between waves and a floater, as shown in Fig. 11 (b). It can be seen that three results are almost the same, only slight differences exist in peaks and troughs.

Table 1 Time step and mesh size details for convergence study without a floating body

Models	Time steps	Mesh size Liquid level encryption zone	Total number of elements	Total time for simulation
1	$\Delta t=T/500$	$\Delta z=H_i/20$, $\Delta x=H_i/10$	78008	1.11 h
2	$\Delta t=T/1000$	$\Delta z=H_i/20$, $\Delta x=H_i/10$	78008	2.27 h
3	$\Delta t=T/2000$	$\Delta z=H_i/20$, $\Delta x=H_i/10$	78008	4.18 h
4	$\Delta t=T/1000$	$\Delta z=H_i/40$, $\Delta x=H_i/20$	302820	10.49 h
5	$\Delta t=T/1000$	$\Delta z=H_i/10$, $\Delta x=H_i/5$	20518	0.68 h

Table 2 Time step and mesh size details for convergence study with a floating square box

Models	Time steps	Mesh size Motion encryption zone	Total number of elements	Total time for simulation
A	$\Delta t=T/500$	$\Delta z=H_i/20$, $\Delta x=H_i/10$	85524	4.04 h
B	$\Delta t=T/1000$	$\Delta z=H_i/20$, $\Delta x=H_i/10$	85524	8.83 h
C	$\Delta t=T/2000$	$\Delta z=H_i/20$, $\Delta x=H_i/10$	85524	16.39 h
D	$\Delta t=T/1000$	$\Delta z=H_i/10$, $\Delta x=H_i/5$	53564	5.28 h
E	$\Delta t=T/1000$	$\Delta z=H_i/40$, $\Delta x=H_i/20$	235528	21.16 h

Table 3 Prism layer details for convergence study with a “Berkeley-Wedge” floater

Models	The thickness of prism layer	The number of layers	The value of $y+$
a	$H_i/20$	20	$0.0<y+<0.3$
b	$H_i/20$	10	$0.01<y+<0.8$
c	$H_i/20$	5	$1.4<y+<3.5$

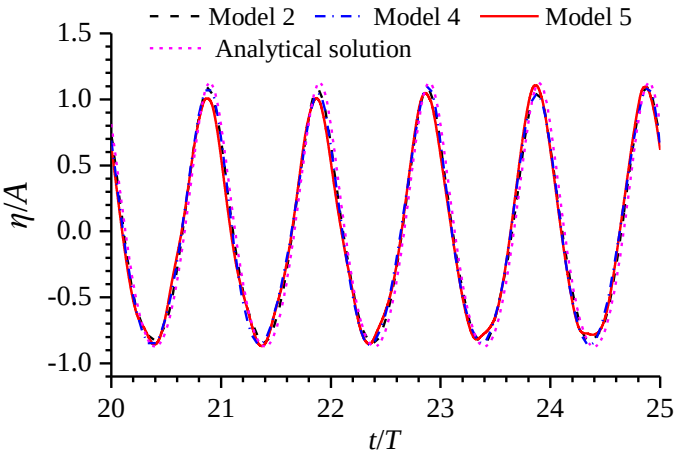

(a) Wave elevations at the centre of wave flume with different meshes.

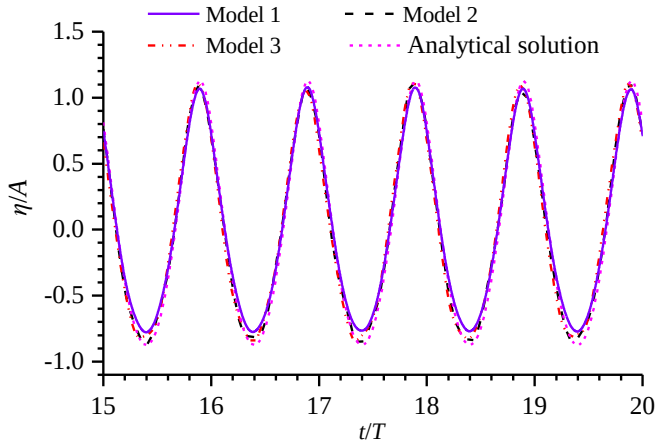

(b) Wave elevations at the centre of wave flume with different time steps.

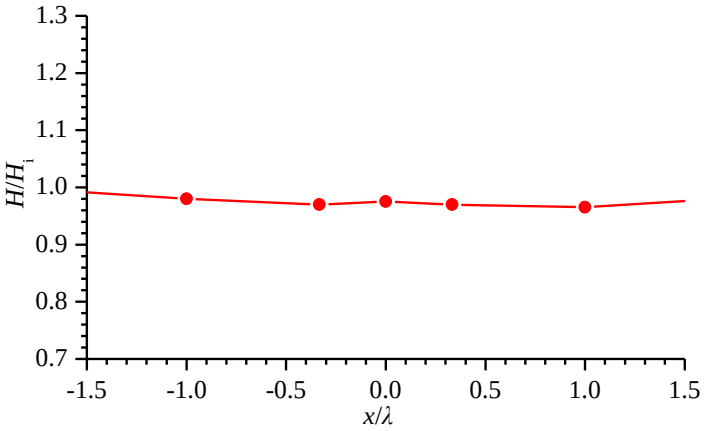

(c) Spatial distribution of wave heights

Fig. 8 Wave elevations at the centre of wave flume and spatial distribution of wave heights without body with H_i=0.2m at T=1.37s.

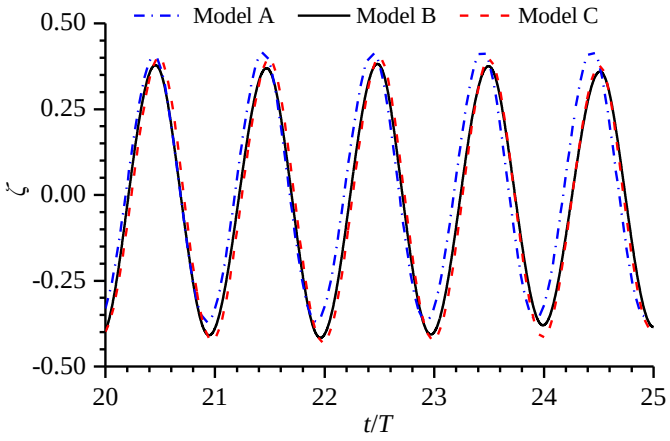

(a) Convergence study for different time steps.

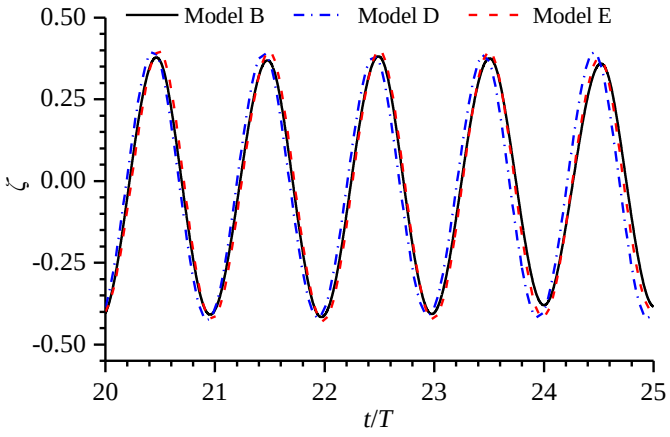

(b) Convergence study with mesh size

Fig. 9 Convergence study with mesh size and time step for heave motion of a floating square box with H_i=0.2m at T=1.37s.

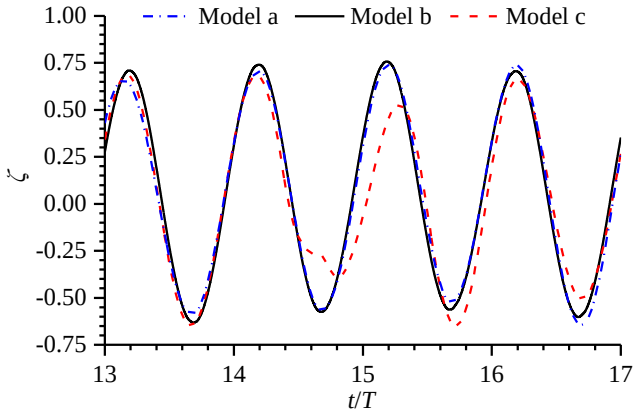

Fig. 10 Convergence study with different y+ of LES turbulence model for heave motion of a "Berkeley-Wedge" floater with H_i=0.0508m at T=1.56s.

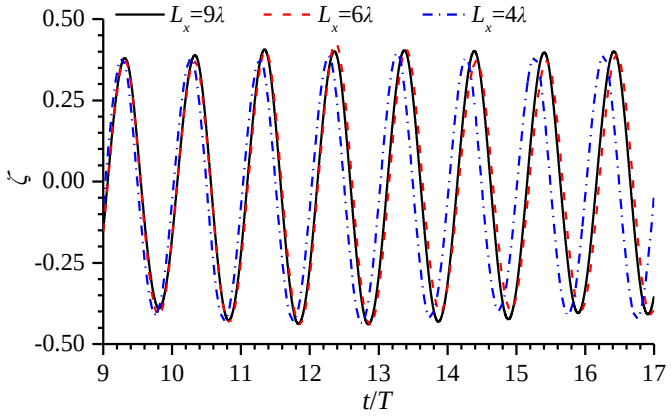

(a) Convergence study with tank length L_x for heave motion.

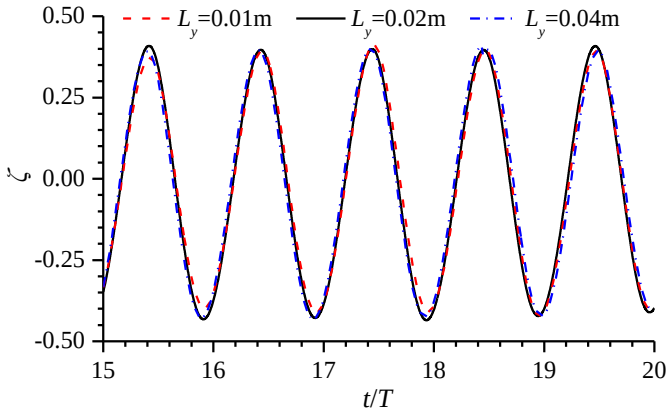

(b) Convergence study with tank width L_y

Fig. 11 Convergence study with tank dimensions for heave motion of a floating square box with H_i=0.2m at T=1.37s.

3.2 Comparison of published experimental and numerical results

Many researchers have validated the Star CCM+ program for applications involving offshore structures design. Westphalen et al. [42] studied the effect of regular waves on a horizontal and vertical fixed cylinder using Star CCM+ program. Bilandi et al. [28] built a two dimensional symmetrical wave tank in Star CCM+ to simulate the problem of asymmetrical wedges entering calm water vertically at constant speed. In order to verify the present CFD model in this paper, experiments of a pile-restrained floating square box in waves by Ning et al. [20] were simulated, with models parameters the same as in the above convergence study, except for the altered width of the floating box B/λ. Fig. 12 compares the present CFD results using the laminar flow model and the large eddy simulation (LES), experiments by Ning et al. [20] and linear analytical results by Zhao et al.[19]. The variations of the heave motion ζ and the transmition coefficient K_t as a function of relative box width B/λ, derived from the present

CFD numerical simulations agree well with Ning et al.'s experiments. A significant difference exists between the linear potential numerical results of Isaacson et al. and the experiment data for $B/\lambda<0.3$, especially around the resonant frequency for the floating box at $B/\lambda=0.22$, where the maximum overestimation is about 52.3% for the heave motion ζ and 35.3% for the transmission coefficient K_t at the resonant frequency. This is because viscous effects provide an important damping effect on floater motion and can not be ignored for a small body relative to the wave length or for a resonant body [21]. Potential flow theory could overestimate the floating body response in such situations, so CFD models are required.

Fig. 13 shows the comparison of heave motion ζ and conversion efficiency η_e of a floating "Berkeley-Wedge" breakwater among the present CFD results, experimental results by Madhi et al. [24] and the linear potential numerical results [35], where the CFD results using the large eddy and laminar flow models are both given for the comparison. The width and draft of the floater were $B/h=0.15$ and $D/h=0.53$, and other detailed parameters can be found in Madhi et al. [24]. The linear potential numerical results overpredict the heave motion and the conversion efficiency, similar to Fig. 12. The maximum overestimation is about 39.1% for the heave motion ζ near $\omega=4.64$ rad/s, which is smaller than those of the floating box. This is because the vortices around the "Berkeley-Wedge" breakwater are smaller, which will be further discussed in the following section. The CFD results calculated by the LES model agree well with the experimental results of Madhi et al., while the laminar flow model overestimates the results in the high frequency region. The maximum overestimation is about 20.4% for the heave motion ζ and 34.3% for the conversion efficiency η_e. The heave motion and therefore the strength on the vortex shedding that develops at corners increases as the width of the body decreases. For this "Berkeley-Wedge" breakwater with $B/h=0.15$, the heave motion is larger and the width is smaller than the floating box with $B/h=0.8$. The width of the "Berkeley-Wedge" breakwater is increased to $B/h=0.33$ to study this effect. The results are shown in Fig. 14. It can be seen that the results obtained by the laminar flow and LES models are almost the same, which means that increasing the body width reduces the impact of vortex shedding on body motion. Therefore, when the width of the body is relatively large, the laminar flow model is sufficient. But for bodies with relatively small width, the laminar flow model is insufficient. The overall agreement between the present CFD results and the published experimental data verifies the present CFD model can accurately predict the interaction of regular waves with floaters of arbitrary shape. In this paper, the laminar flow model or the LES model is used according to the width of the body, for the balance of accuracy and efficiency.

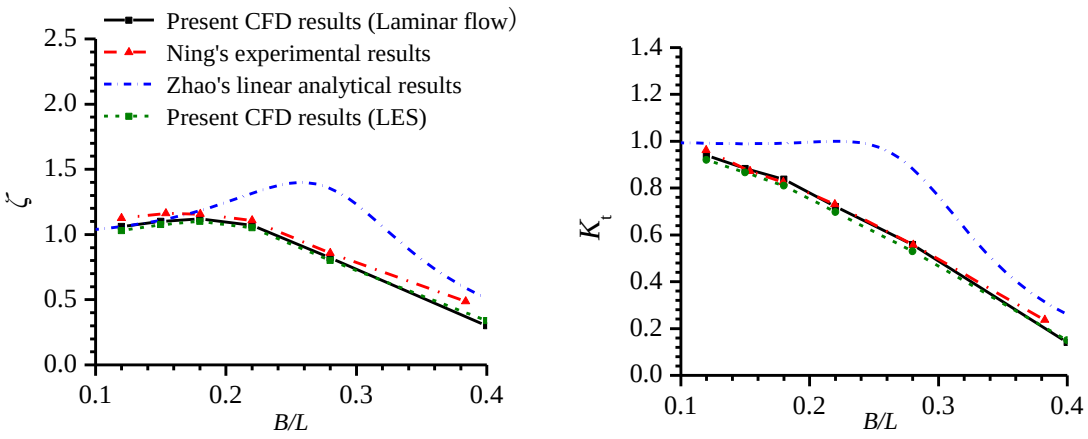

(a) Heave motion (b) Transmission coefficient

Fig. 12 Comparisons of ζ and K_t vs. normalised floater width between the present laminar flow and LES CFD results, Ning et al.'s experiments and Isaacson's potential results for a floating square box.

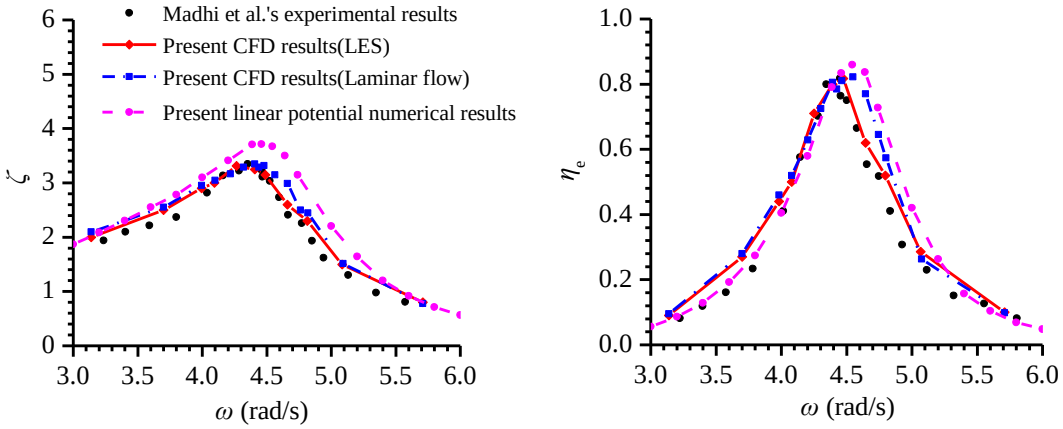

(a) Heave motion (b) Conversion efficiency

Fig. 13 Comparisons of ζ and η_e between the present CFD results and Madhi et al.'s experimental results for the Berkeley-Wedge floater.

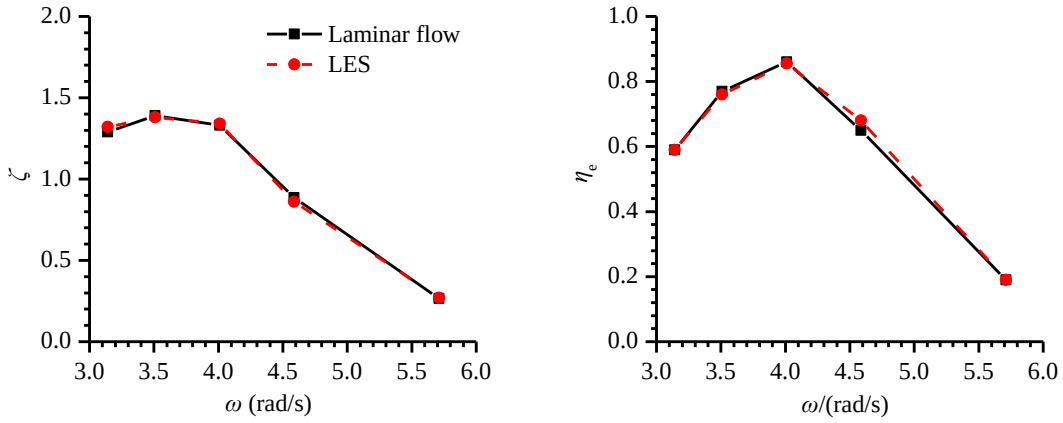

(a) Heave motion (b) Conversion efficiency

Fig. 14 Comparisons of ζ and η_e between the present laminar flow CFD results and large eddy simulation results for the Berkeley-Wedge floater with B/h=0.33 and D/h=0.53.

3.3 Verification of optimal PTO damping

In the following cases, the optimal PTO damping coefficient will be determined. The first step is to verify the accuracy of Eq. (6) based on potential flow theory as compared with the CFD results. For the box-type floating breakwater in Fig. 9, the natural frequency ω_n=4.22 rad/s and the optimal damping coefficient b_{opt}=9.75 kg/s were obtained based on Eqs. (5) and (6), respectively. Fig. 15 shows the variation of conversion efficiency of the floating box as a function of PTO damping coefficient at ω_n=4.22 rad/s. Conversion efficiency is maximised when b/b_{opt}=1, as shown in Fig. 15, illustrating that potential flow theory provides an accurate method for determining the optimal damping b_{opt}. In the following cases, the optimal damping coefficients are obtained firstly based on Eq. (6), and then input into the present CFD models for maximum wave energy capture.

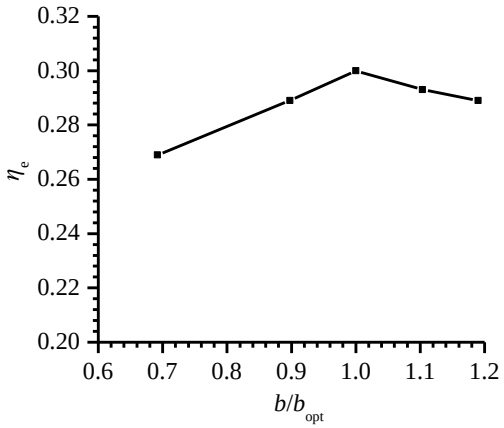

Fig. 15 Variations of η_e versus PTO damping coefficient of floating box-type breakwater with B/h=0.6 and D/h=0.2 at ω_n=4.22 rad/s.

4. Performance of the integrated system

As an integrated system of WECs and breakwaters, the hydrodynamic performance including wave attenuation and energy extraction are very important. The wave transmission characteristic is an important consideration of the functional role of a breakwater, with smaller transmission coefficients preferred. Ning et al. [16] and Madhi et al. [24] studied the hydrodynamic performance of an integrated system where the floater had a square bottom and a Berkeley-Wedge bottom, respectively, and showed that the shape of the bottom of the floater was a significant factor in the hydrodynamic performance of the integrated system, as did the width and draft of the floaters. Therefore, the effects of bottom shape, relative width and draft on the hydrodynamic performances are investigated below. Ning et al. [16] showed the transmission coefficient K_t decreased with the increasing of PTO damping. The change in K_t reduced significantly when the PTO damping was larger than the optimal PTO damping,

while the PTO damping had a large influence on the wave energy conversion efficiency. Therefore, the optimal PTO damping is chosen for all cases in present study to obtain acceptable wave attenuation performance and efficient wave energy conversion.

4.1 Effect of floater bottom shape

This section studies the influence of floater bottom shape on wave energy extraction performance as a wave energy converter and wave attenuation performance as a breakwater. As shown in Fig. 16, four different bottom shapes were considered, they are: square bottom, triangular bottom, Berkeley-Wedge bottom and triangular-baffle bottom. Their width B/h=0.5 and displacement V=0.204m^3 were kept the same. The mass of the floaters is equal to their displacements, so their mass is also the same. Except for the floater with square bottom, the top vertical sections under the water surface of the other floaters were all D_1/h=0.15. The thickness of the baffle in the triangular-baffle bottom model was B_1/h=0.01325. The other parameters can be found in Fig. 16. The incident wave height was H_i/h=0.1 and the water depth was h=2.0m.

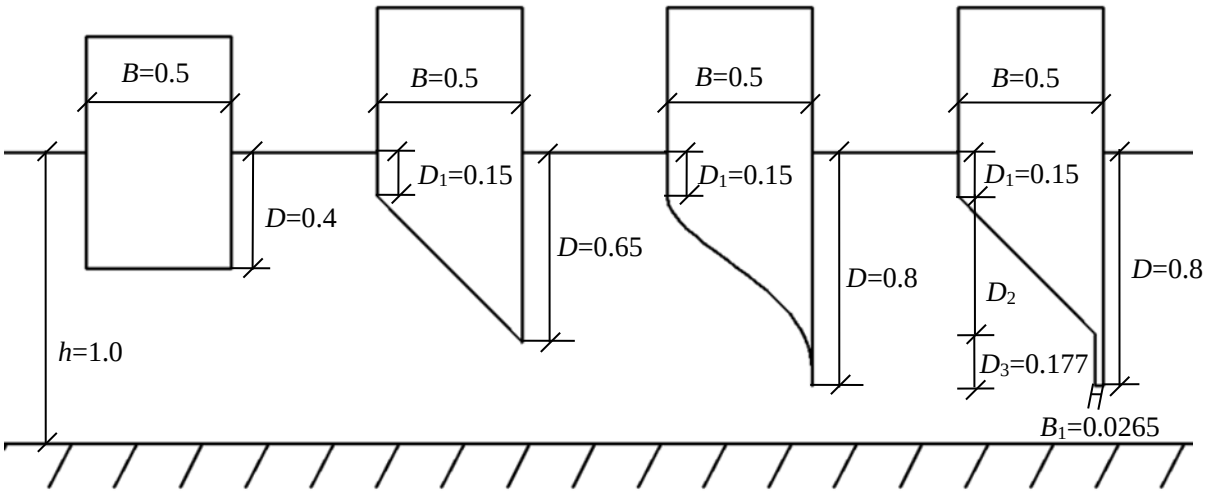

(a) Square bottom (b) Triangular bottom (c) Berkeley-Wedge bottom (d) Triangular-baffle bottom

Fig. 16 Schematic diagram of four floaters with different bottom shapes (Unit: m).

Fig. 17 shows the variation of heave motion ζ, conversion efficiency η_e, transmission coefficient K_t, reflection coefficient K_r and dissipation coefficient K_d with wave frequency for the four floaters. Fig. 18 shows the vorticity fields around the four floaters with different bottom shapes, at the resonance frequency and with the optimal PTO damping. It can be seen from Fig. 17, the variation trends of heave motion ζ, conversion efficiency η_e and transmission coefficient K_t for these four floaters are similar. The conversion efficiency η_e reaches the maximum value at the resonant frequency. The transmission coefficient K_t decreases with increasing wave frequency, implying that the wave attenuation performance of the floaters is better for short waves than long waves. In the frequency range of 3.0<ω<4.5

rad/s, the conversion efficiency η_e of the Berkeley-Wedge floater is the largest with a maximum conversion efficiency of 87%, and the transmission coefficient K_t is the lowest. As expected, the conversion efficiency of the floater with square bottom is much lower than the other three floaters at all wave frequencies, even lower than 50%. This is because the wave energy consumed by the heave of the floater with square bottom is largest, as shown in Fig. 17 (e). Comparing Fig. 18 (a) and (c), it can be seen that much stronger vortices develop near the corner of the square bottom than the Berkeley Wedge bottom throughout the whole wave period. Consequently, more energy is dissipated for the square bottom. Hence less energy will be extracted by the PTO by the square bottom floater, whereas the Berkeley Wedge, with little energy dissipation into the fluid, extracts the most energy. Weaker vortices develop because of the smooth curved bottom. Therefore most energy is absorbed by the PTO, leading to the largest conversion efficiency in Fig. 17 (b). Furthermore, the transmission coefficient K_t of the square bottom floater is much higher than the Berkeley Wedge floater for ω<4.5 rad/s. The square bottom floater generally has the worst wave energy extraction performance as a WEC and the worst wave attenuation performance as a breakwater.

In practice, the Berkeley-Wedge bottom is not easy to manufacture due to the curved geometry of the bottom. Therefore, it may be advantageous to investigate other bottom shapes with similar wave energy extraction and wave attenuation performances as a simpler alternative. Firstly, a triangular bottom with the same weight and smaller draft is considered. From the comparison of floaters with Berkeley-Wedge bottom and triangular bottom shown in Fig. 17, it can be seen that the results for ω>4.5 rad/s are almost the same, while for ω<4.5 rad/s, the conversion efficiency η_e of the floater with the triangular bottom is less than that of the floater with the Berkeley-Wedge bottom, and the transmission coefficient K_t is much larger. This is closely related to the attenuation rate of water particle velocity due to wave motion. Because the velocity of water particles decay with water depth, its effect on the transmission coefficient becomes smaller along the water depth. Additionally, the energy of the wave decreases with the water depth, so the deeper the device goes, the more of the available wave energy it will interact with and the larger the radiation damping, which leads to the larger conversion efficiency η_e for the floater with the Berkeley-Wedge bottom. For the short waves in the region ω>4.5 rad/s, the water particle velocity decays much faster than the long waves along the water depth, as shown in Fig. 19 (a). Therefore, when the draft exceeds a certain depth, there is little effect on the body motion and the transmission coefficient. On the contrary, for long waves ω<4.5 rad/s, the water paticle velocity decays more slowly with water depth, as shown in Fig. 19 (b). Consequently, the effect of the draft on the body motion and the transmission coefficient is significant. Smaller draft results in a larger transmission

coefficient and smaller body motion, which can also explain the large value of transmission coefficient for the square box in the region ω<4.5 rad/s.

Based on the above analysis, the draft of the body is considered to be the main influence parameter. Therefore, to improve the hydrodynamic performance of the floater, a modified design is developed by adding a thin baffle to the floater with the triangular bottom to keep the same draft as the Berkeley-Wedge bottom, as shown in Fig. 16 (d), which is called the triangular-baffle bottom floater. It can be seen from Fig. 17, the performance of the floater with the triangular-baffle bottom is very similar to that with the Berkeley-Wedge bottom, not only improving wave attenuation performance, but also the power generation performance is greatly enhanced. As shown in Fig. 17 (c), the transmission coefficient k_t of the floater with triangular-baffle bottom are almost the same as those with the Berkeley-Wedge bottom because the two floaters have the same draft. From Fig. 17 (a) and Fig. 17 (b), it can be seen that only a slight difference exists between the conversion efficiency of the floater with Berkeley-Wedge bottom and that with the triangular-baffle bottom, as with the heave motion. The maximun conversion efficiencies of those two floaters at resonance frequency are 86.7% and 82.5%, respectively. As shown in Fig. 18 (c) and (d), when these two floaters are moving in heave motion, only small vortices are shed near the corner and the tip of the bottom. The dissipation energy is dominated by the vortex shedding at the edge of the floater. Therefore, the stronger the vortex shedding in Fig. 18, the larger the dissipation coefficients k_d in Fig. 17 (e). Through energy conservation, as less energy of the Berkeley-Wedge bottom and triangular-baffle bottom floaters is reflected, transmitted and dissipated than the square bottom floater, more energy is absorbed by the PTO system.

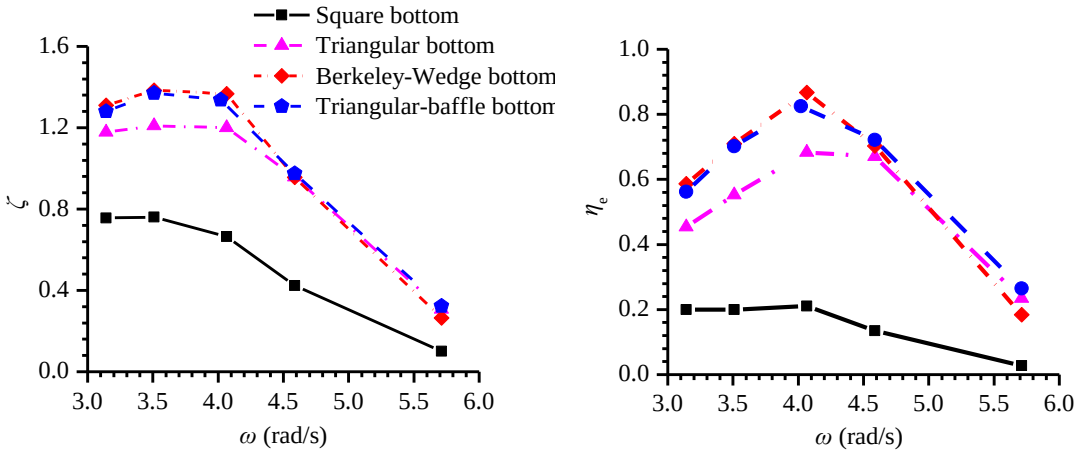

(a) Heave motion

(b) Conversion efficiency

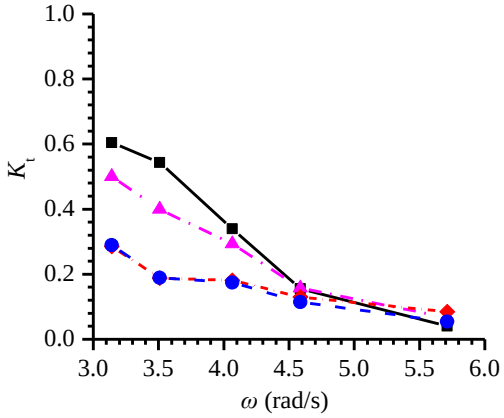

(c) Transmission coefficient

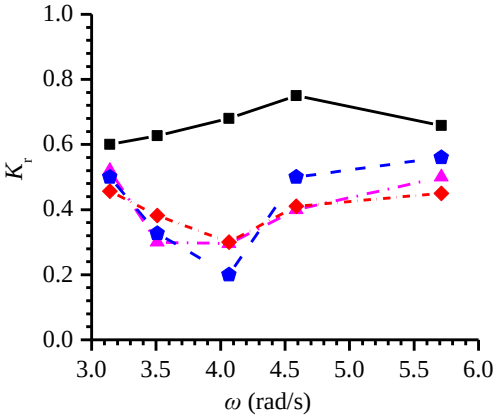

(d) Reflection coefficient

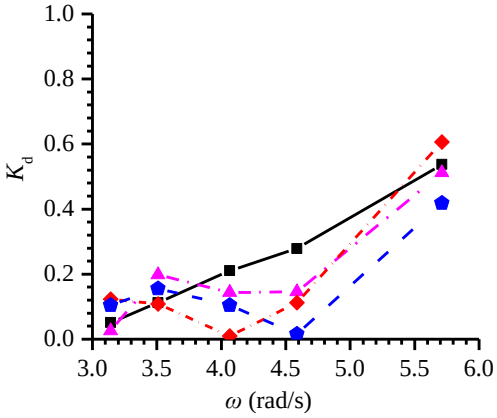

(e) Dissipation coefficient

Fig. 17 Variations of ζ, η_e, K_r, K_t and K_d versus ω for different bottom shapes and with the same displacement under the optimal PTO damping.

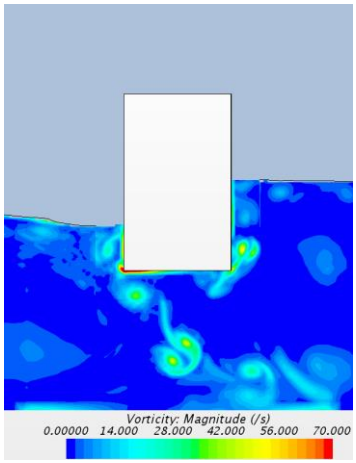

t=*NT*

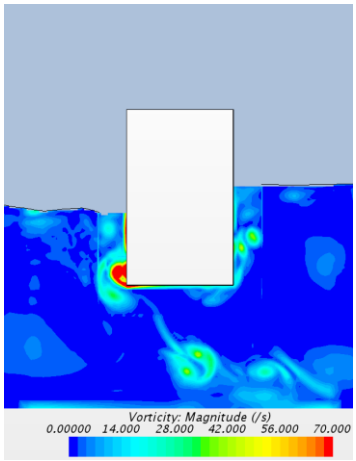

t=*NT*+*T*/6

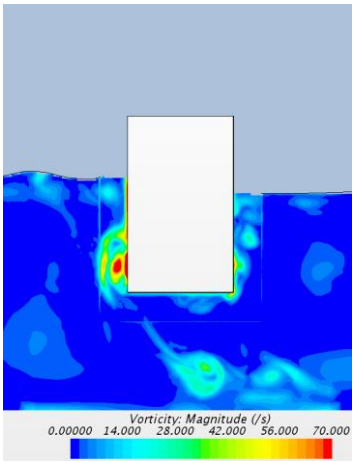

t=*NT*+*T*/3

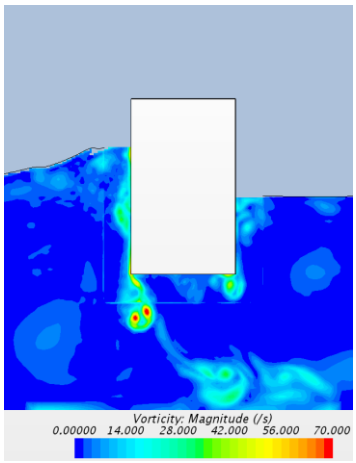

t=*NT*+ *T*/2

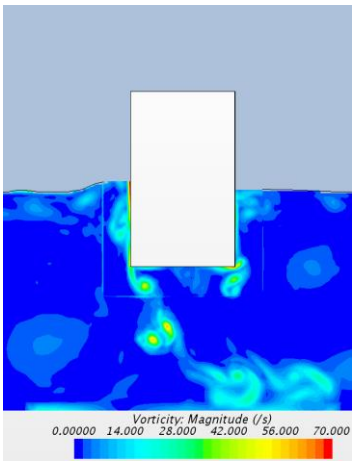

t=*NT*+2*T*/3

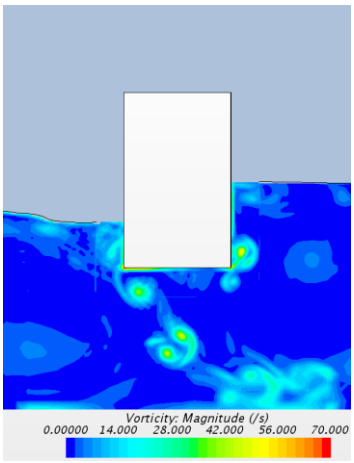

t=*NT*+5*T*/6

(a) Square bottom

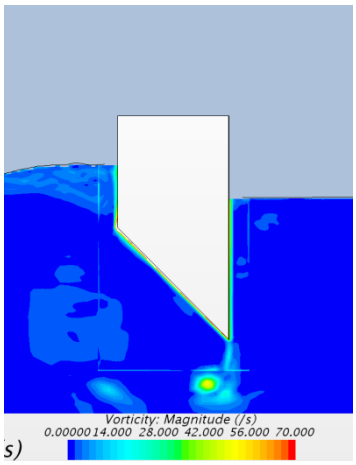

t=*NT*

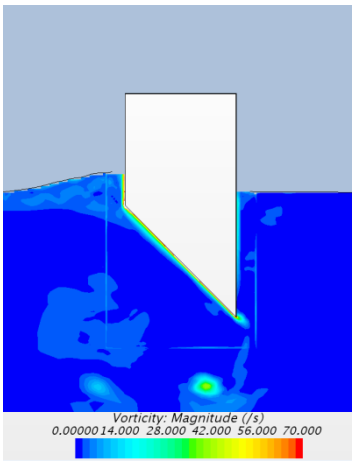

t=*NT*+*T*/6

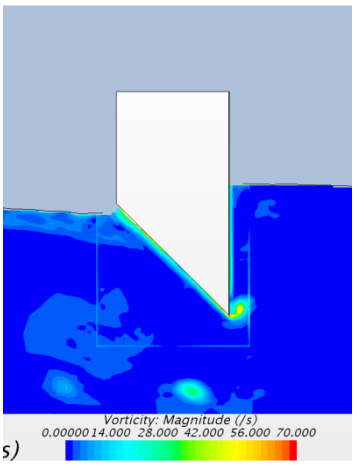

t=*NT*+*T*/3

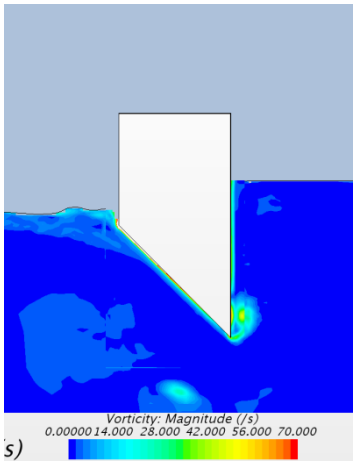

t=*NT*+*T*/2

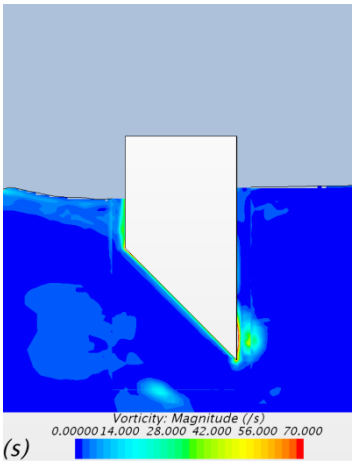

t=*NT*+2*T*/3

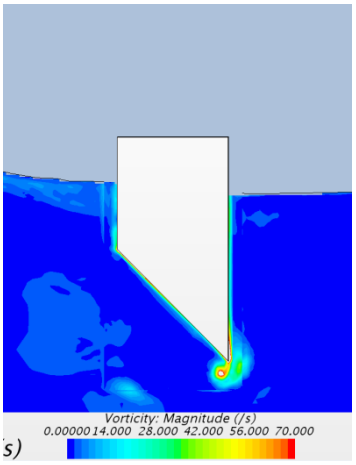

t=*NT*+5*T*/6

(b) Triangular bottom

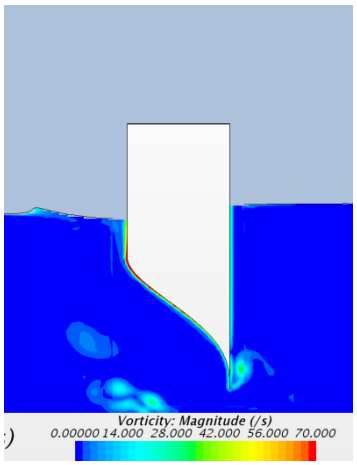

t=*NT*

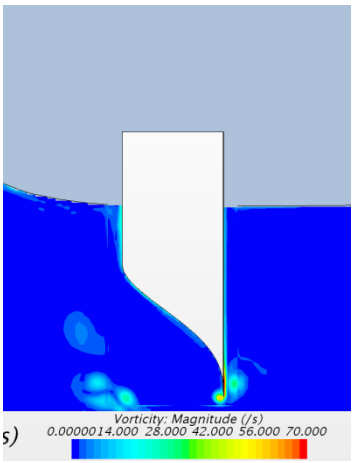

t=*NT*+*T*/6

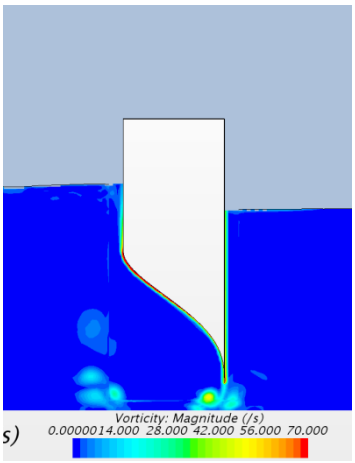

t=*NT*+*T*/3

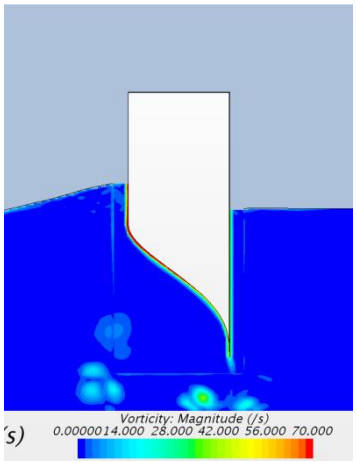

t=*NT*+*T*/2

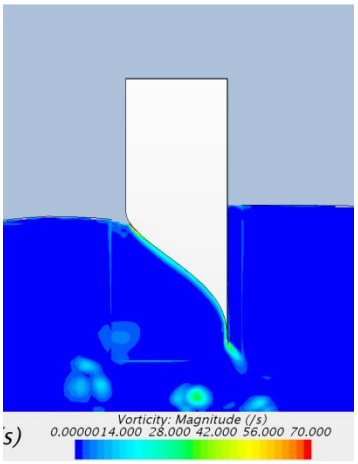

t=*NT*+2*T*/3

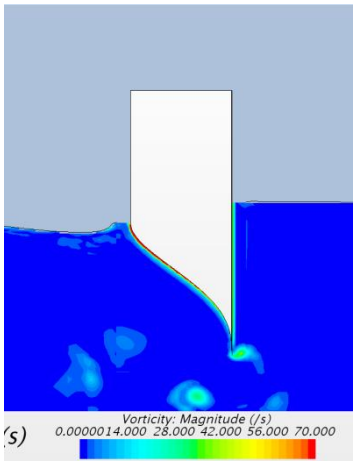

t=*NT*+5*T*/6

(c) Berkeley-Wedge bottom

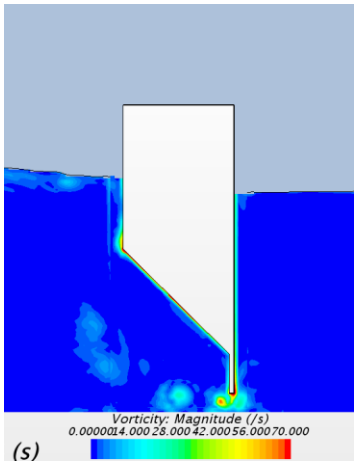

t=*NT*

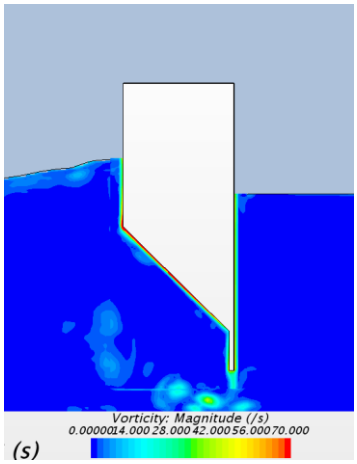

t=*NT*+*T*/6

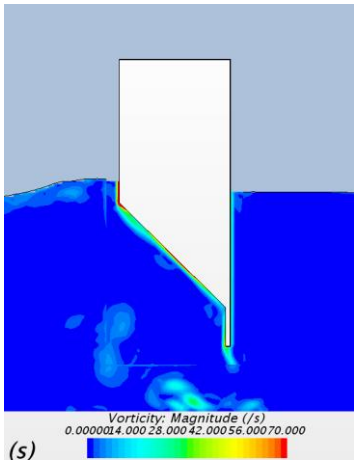

t=*NT*+*T*/3

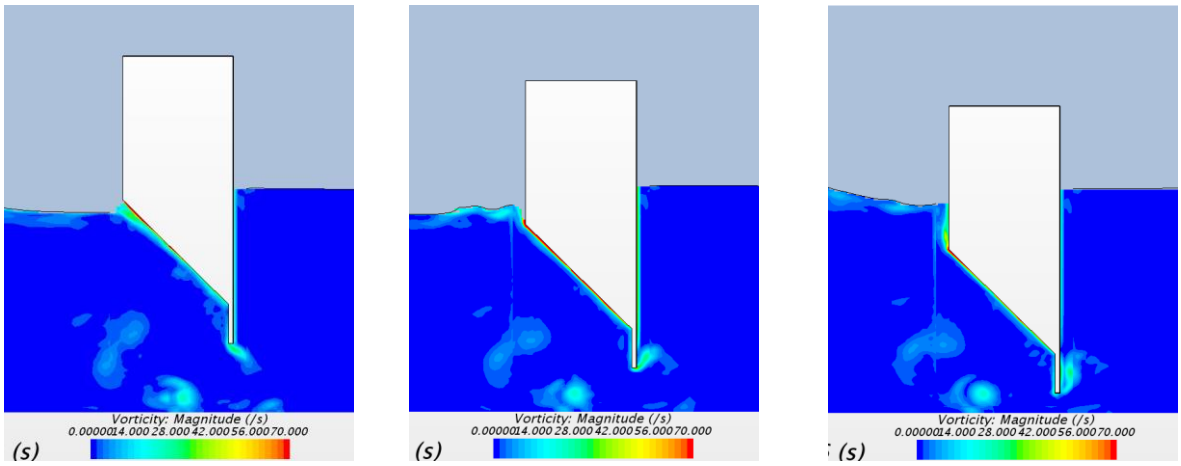

$t=NT+T/2$ $t=NT+2T/3$ $t=NT+5T/6$

(d) Triangular-baffle bottom

Fig. 18 Vorticity field around the floaters with different bottom shapes.

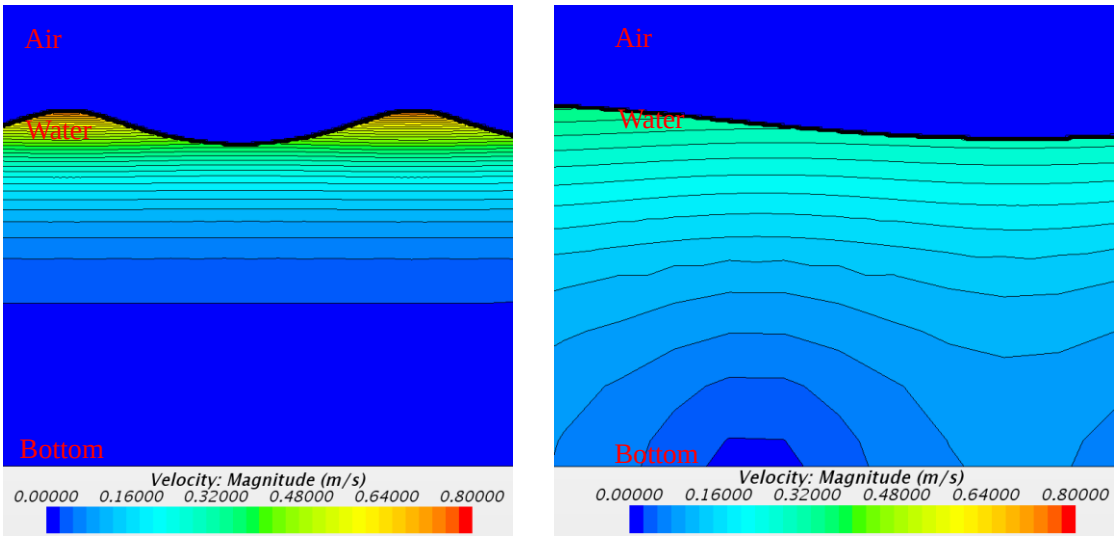

(a) ω=5.71rad/s (b) ω=3.14rad/s

Fig. 19 Variation of water particle velocity along the water depth for ω=5.71rad/s and ω=3.14rad/s

From the above comparison, it can be seen that the integrated system with Berkeley-Wedge bottom offers superior wave attenuation and energy extraction performance. A similar conclusion is drawn by Madhi et al. [24], who investigated an asymmetric energy-capturing floating breakwater with potential flow theory and experiments. However, it should be noted that the performance of the Berkeley-Wedge type device can be closely approximated by the simpler triangular-baffle bottom, which offers significant improvements over that of the triangular bottom model. In particular, the wave attenuation and energy extraction performance of triangular-baffle bottom model are almost the same as those of the floater with Berkeley-Wedge bottom, and slightly better performance is observed in the high frequency region. For practical engineering applications, the triangular-baffle bottom floater may be geometrically simpler to manufacture than a Berkeley-Wedge bottom floater, which means the

manufacturing cost of the triangular-baffle bottom floater is lower than that of the Berkeley-Wedge bottom floater. Thus, the results in this section provide an alternative geometric shape of the floater for practical design to improve the economic competitiveness of WECs. We further analyze the triangular-baffle bottom model to provide guidance for optimizing its geometric shape for real applications.

4.2 Effect of floater width B/h

For the purpose of investigating the effect of relative width B/h on the hydrodynamic performance of triangular-baffle-type floating breakwater, four different relative widths of B/h=0.35, 0.25, 0.15 and 0.1 were investigated, where the draft of the floater was kept constant at D/h=0.4. The other parameters were unchanged at D_1/h=0.075, D_2/h=0.2365, D_3/h=0.0885, A/h=0.05 and h=2.0m. Fig. 20 shows the variation of heave motion ζ, conversion efficiency η_e, transmission coefficient K_t, reflection coefficient K_r and dissipation coefficient K_d of the integrated system against wave frequency for different widths.

It can be seen from Fig. 20 (a) that the heave motion of the floater increases with decreasing floater width for all frequencies. The decrease in relative width leads to a reduction in the mass and added mass of the floater, and consequently the heave motion will be larger for an incident wave of a given size. In other words, larger floaters experience smaller heave motions. Consequently, the resonant frequency of the floater increases with decreasing floater width. Fig. 20 (b) shows that the peak value of conversion efficiency increases firstly and then decreases as the floater width increases. The maximum peak value of conversion efficiency η_e reaches 85.1% at B/h=0.15, although the maximum η_e at B/h=0.25, 80.0%, and the conversion efficiency decreases from this peak more slowly over a broader range of wave frequencies. The peak value of conversion efficiency moves towards the higher frequency region as the width decreases, following the upwards trend in resonant frequency with relative width. It can be seen from Fig. 20 (c) that the transmission coefficient K_t increases slightly as the width increases. This is because the transmission coefficient is closely related to the draft, and the drafts of these four models with different relative widths are kept constant. From Fig. 20 (d), it can be seen that the reflection coefficient of the floater with B/h=0.25 is larger than those of the other three floaters, and in the region ω<4.0 rad/s, the reflection coefficient increases with the decrease of the floater width B/h. This is because the greater the inclination angle of the wall, the weaker the wave reflection ability. With the increase of the relative width B/h, the inclination angle of the triangular part D_2 increases, resulting in the reduction of the wave reflectivity of the floater. The dissipation coefficient decreases with the decrease of the floater width B/h in the region ω>3.4 rad/s, as shown in Fig. 20 (e). This is because stronger vortices develop at corners with smaller angles, which results in more energy dissipation, as shown in

Fig. 18.

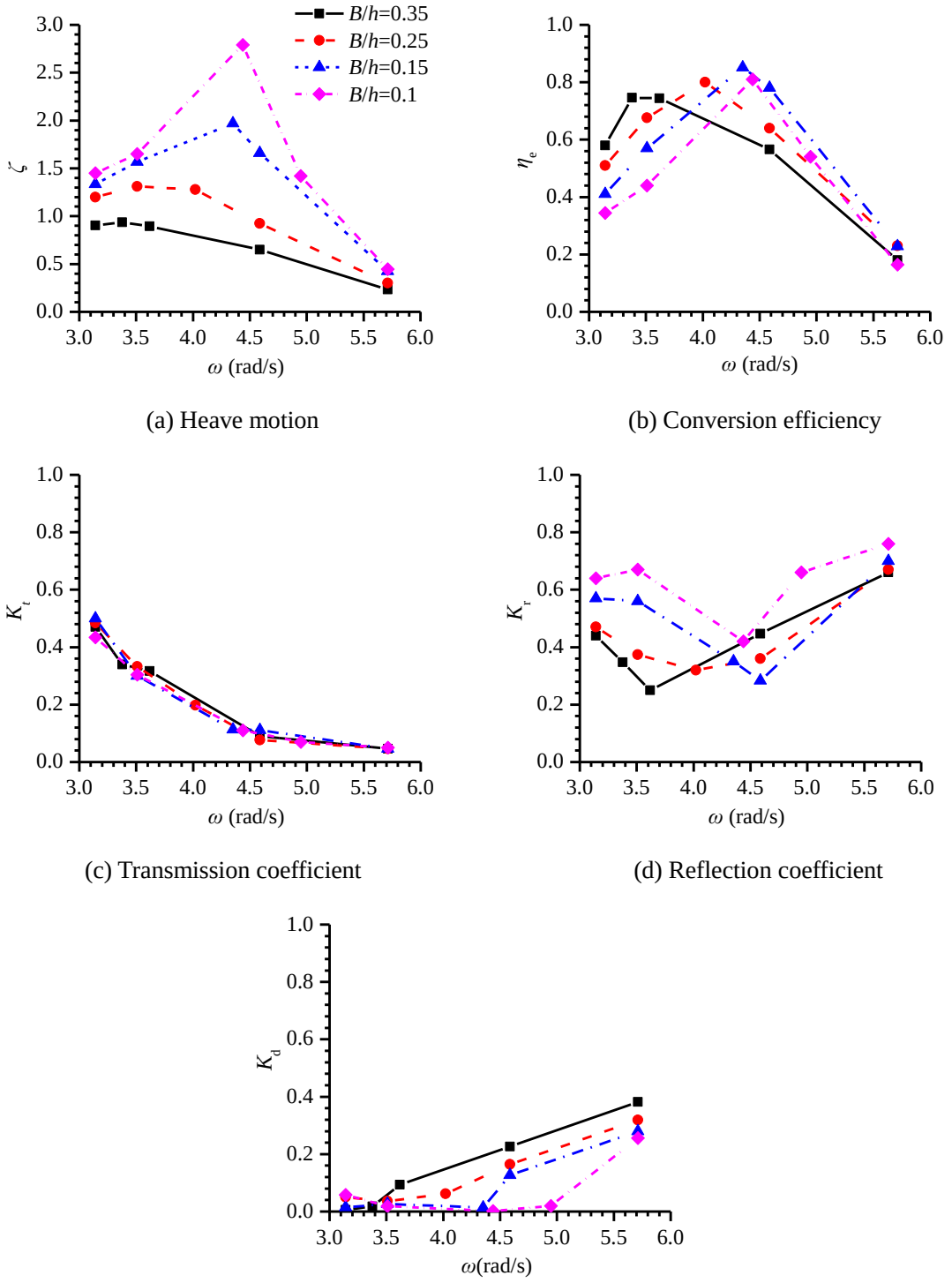

Fig. 20 Variations of ζ, η_e, K_t, K_r and K_d versus ω for the triangular-baffle bottom floater with different relative widths and the same relative draft D/h=0.4.

4.3 Effect of ratio of triangular wedge geometry D_1/D

The triangular-baffle bottom includes the upper vertical side D_1, the triangular part D_2 and

the lower vertical baffle part D_3. The lower vertical baffle part D_3 was designed to improve the hydrodynamic performance of the floater, as verified in Fig. 17. The upper vertical side D_1 was designed to keep the same displacement with the floater with the Berkeley-Wedge bottom, which also provides smooth water entry. Therefore, it is necessary to investigate the effect of the upper vertical side D_1 on the hydrodynamic performance of the floater. We cut off the upper vertical side D_1 and keep the triangular part D_2 the same with the original D_1 plus D_2, i.e., D_1/D=0, D_2/h=0.3115, as compared with the original design D_1/D=0.1875 and D_2/h=0.59125. Furthermore, another two floaters with D_1/D=0.09375, D_2/h=0.0.59125 and D_1/D=0.28125, D_2/h=0.59125 were also investigated. The total drafts of the floaters were kept as D/h=0.4. The water depth h=2.0m, the width of the floater B/h=0.25 and the incident wave height H_i/h=0.1 were considered. The corresponding masses were 168.8kg, 168.25kg, 203.8kg and 239.4kg for D_1/D=0, D_1/D=0.09375, D_1/D=0.1875 and D_1/D=0.28125, respectively. Fig. 21 shows the variation of heave motion ζ, conversion efficiency η_e, transmission coefficient K_t, reflection coefficient K_r and dissipation coefficient K_d of the integrated system against wave frequency for two different ratios of D_1/D_2.

It can be seen from Fig. 21 that for the heave motion and the conversion efficiency, the results of these four floaters with different ratios of D_1/D for ω<3.8 rad/s are very close, while the results increase with the decrease of the ratio D_1/D ratio in the high-frequency region ω>4.2 rad/s, which is not only because of the reduction of the mass of floater but also the decrease of the ratio of D_1/D. The increase of the reflection coefficient K_r and the decrease of the transmission coefficient K_t with the increase of the ratio of D_1/D may occur because the wave attenuation performance of the vertical section of the floater is better than the triangle near the free surface, especially for the short waves in the high frequency region ω>4.5 rad/s. This is because the wave energy of the short waves is concentrated near the free surface and decays faster along the water depth than the long wave, as shown in Fig. 19. Moreover, it can be seen from Fig. 21 (b) that the maximum peak value of conversion efficiency reaches 92.0% for D_1/D=0.0, compared to 81.0% for D_1/D=0.09375, 80.0% for D_1/D=0.1875 and 75.5% for D_1/D=0.28125. This may arise due to the reduced floater mass as well as the additional vortex that appears at the corner of the upper vertical side D_1 and the triangular part D_2 of the floater, compared to the floater with D_1/D=0, as shown in Fig. 22. This means more energy is dissipated for the floaters with D_1/D>0 compared with the floater with D_1/D=0.0, hence the reduction in dissipation coefficient. The decrease of the reflection coefficient with the decrease of the ratio D_1/D occurs when ω>3.7 rad/s because the wave reflection performance of the vertical section of the floater is better than the triangle section. Although the transmission coefficient K_t of the floater without the upper vertical part D_1/D=0.0 increases

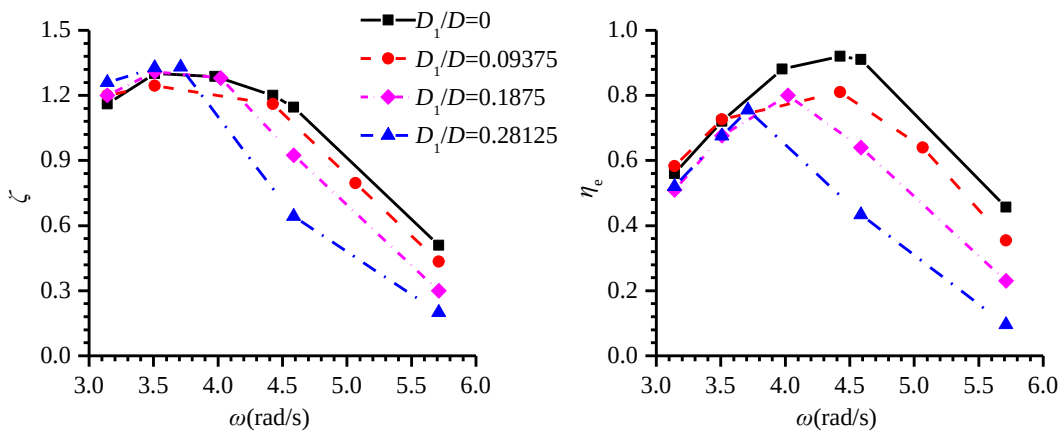

(a) Heave motion

(b) Conversion efficiency

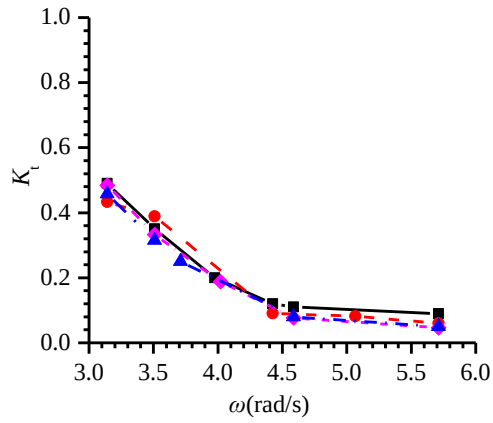

(c) Transmission coefficient

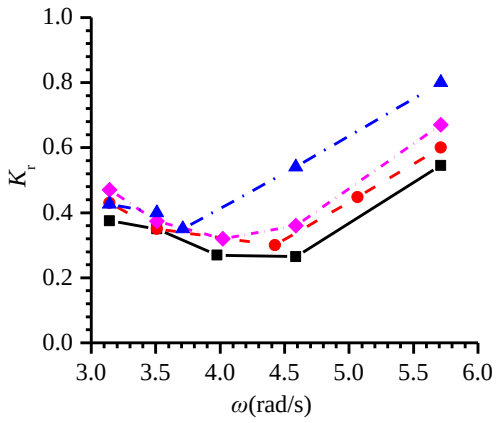

(d) Reflection coefficient

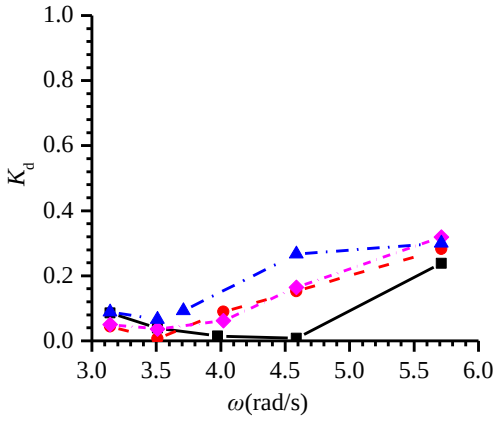

(e) Dissipation coefficient

Fig. 21 Variations of ζ, η_e, K_t, K_r and K_d versus ω for the triangular-baffle bottom floater with different ratios of D_1/D_2 and the same relative draft D/h=0.4.

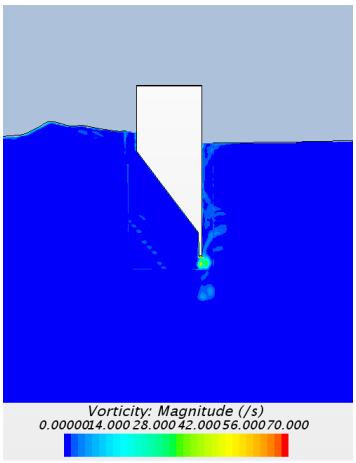

t=*NT*

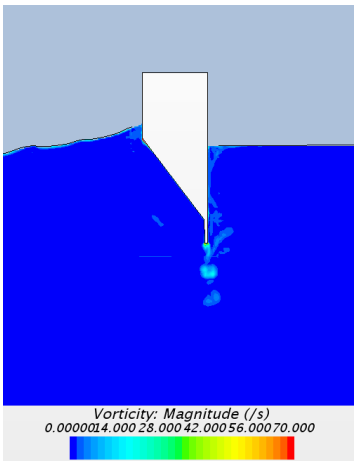

t=*NT*+*T*/6

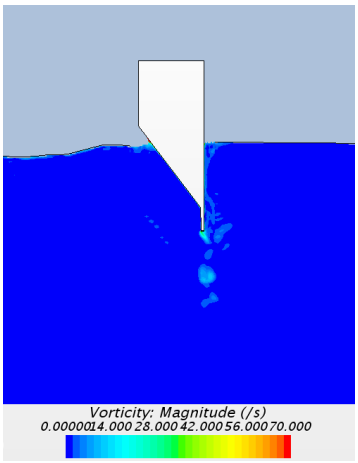

t=*NT*+*T*/3

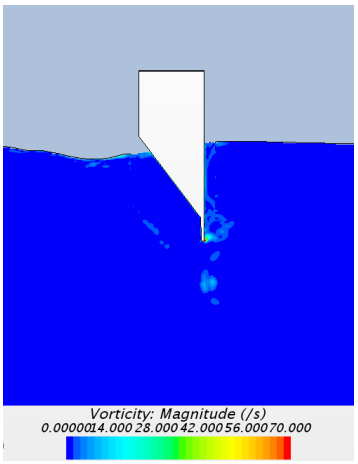

t=*NT*+*T*/2

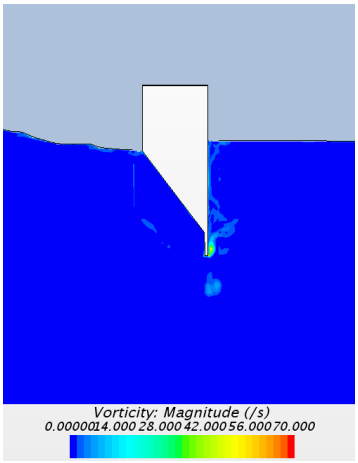

t=*NT*+2*T*/3

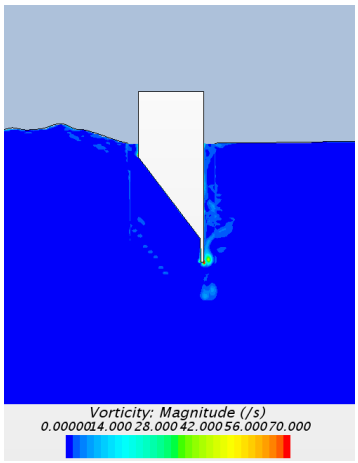

t=*NT*+5*T*/6

(a) Triangular-baffle bottom with D_1/ D_2=0.0

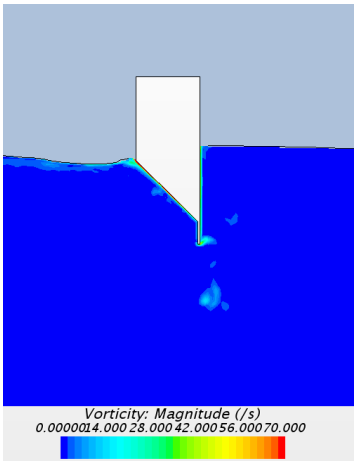

t=*NT*

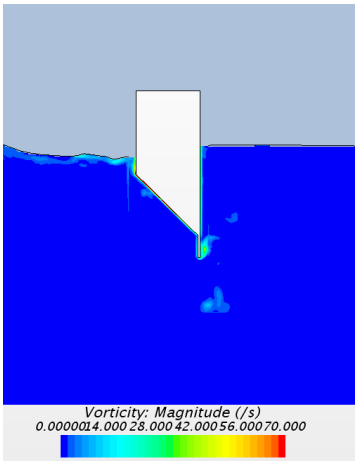

t=*NT*+*T*/6

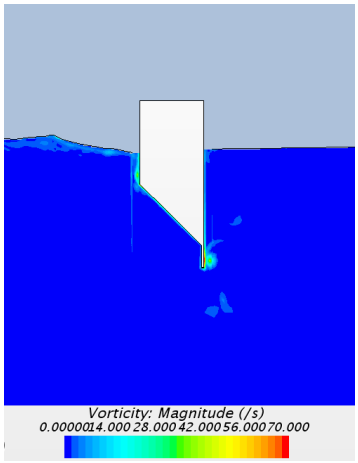

t=*NT*+*T*/3

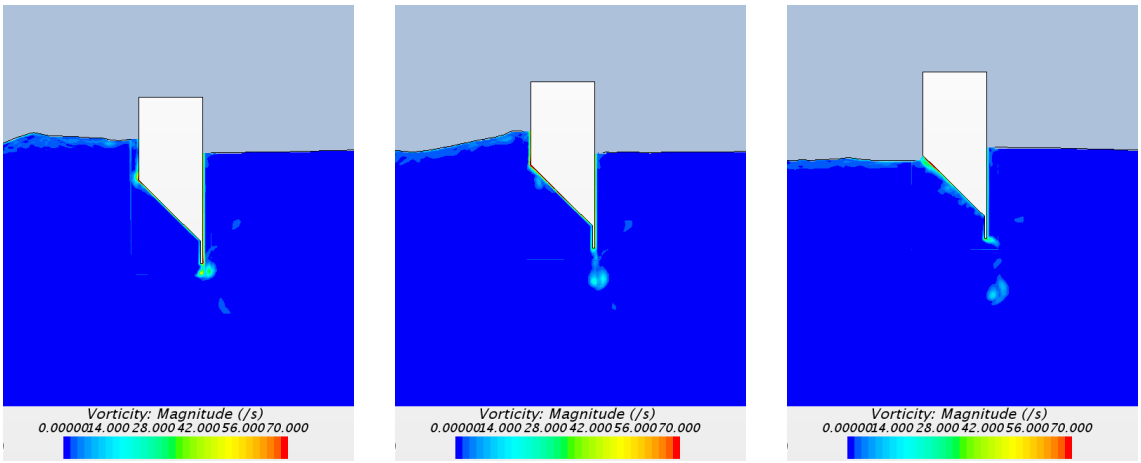

$t=NT+T/2$ $t=NT+2T/3$ $t=NT+5T/6$

(b) Triangular-baffle bottom with D_1/D=0.28125

Fig. 22 Vorticity field around the triangular-baffle bottom floaters with different D_1/D.

almost twice compared with that with the upper vertical part D_1/D=0.28125 in the high frequency region ω>4.5 rad/s, it is still smaller than 0.12, which means the wave attenuation performance is still good. In brief, eliminating the upper vertical side D_1 can increase the energy conversion efficiency and maintain satisfactory wave attenuation performance. Consequently, for a given floater draft, it may be preferable to employ a simple triangle plus baffle geometry in practical engineering applications.

4.4 Effect of ratio of baffle height D_2/D_3

In Section 4.1, it was demonstrated that the lower vertical baffle part D_3 can improve not only the energy extraction performance but also the wave attenuation performance of the floater with triangular-baffle bottom as compared to the floater with triangular bottom. Moreover, the maximum conversion efficiency increases to about 92% by adjusting the ratio of D_1/D_2, as shown in Fig. 21. Therefore, it is worthwhile to study the effects of the ratio of baffle height D_2/D_3 on the hydrodynamic performance. For this purpose, three triangular-baffle bottom models with ratios of D_2/D_3=1.3466, 2.6723 and 7.4416 were investigated. The ratio of D_1/D_2=0.1875, water depth h=2.0m, floater width B/h=0.25, total floater draft D/h=0.4 and incident wave height H_i/h=0.1 were considered. The corresponding mass was 227.6kg, 203.8kg and 180.1kg for D_2/D_3=7.4416, 2.6723 and 1.3466, respectively. Fig. 23 shows the variation of heave motion ζ, conversion efficiency η_e, transmission coefficient K_t, reflection coefficient K_r and dissipation coefficient K_d of the integrated system against wave frequency for the different ratios of D_2/D_3.

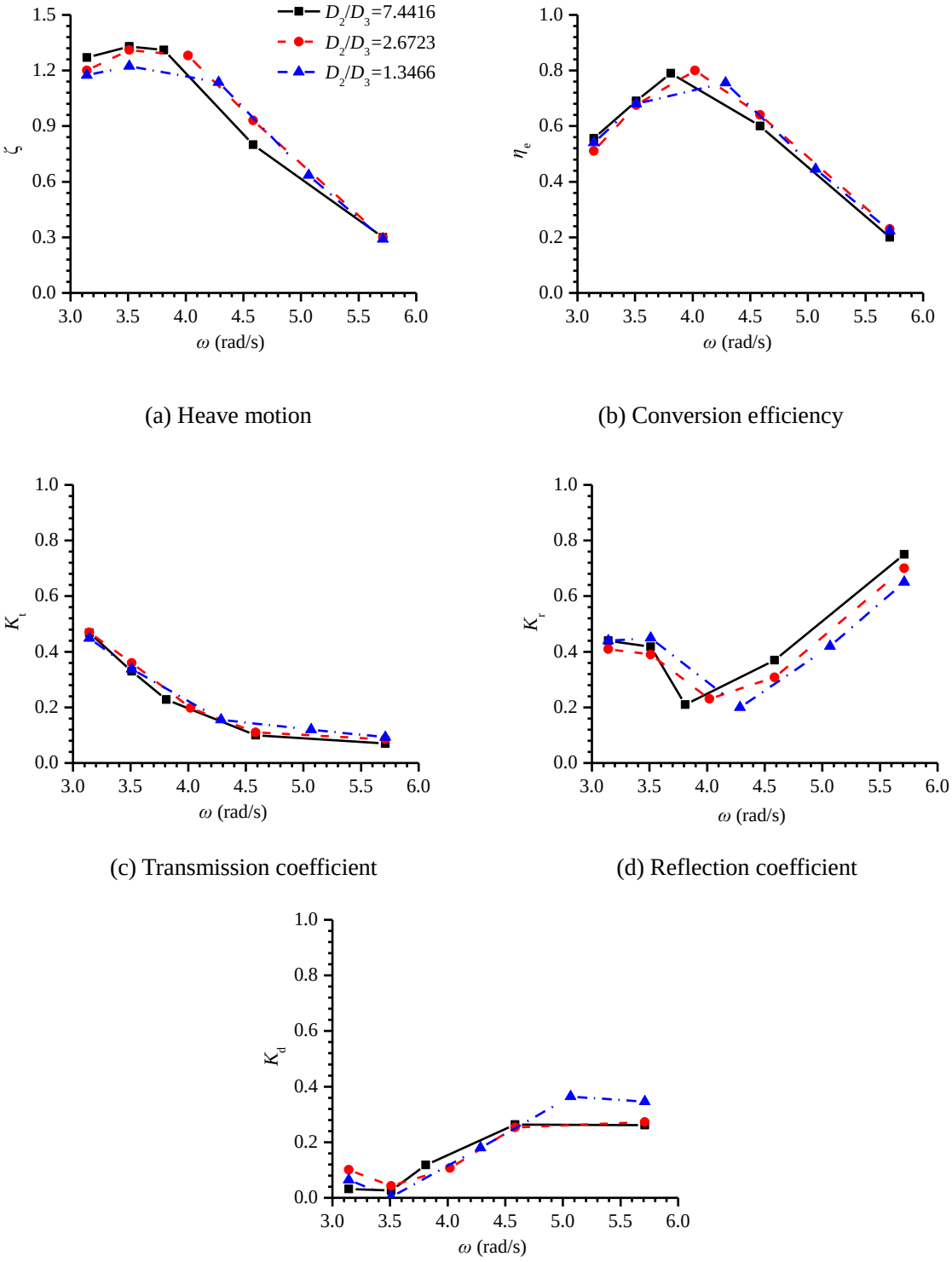

(a) Heave motion

(b) Conversion efficiency

(c) Transmission coefficient

(d) Reflection coefficient

(e) Dissipation coefficient

Fig. 23 Variations of ζ, η_e , K_t, K_r and K_d versus ω for the triangular-baffle bottom floater with different ratios of D_2/D_3 and the same relative draft D/h=0.4.

It can be seen from Fig. 23 that the heave motion ζ, conversion efficiency η_e and transmission coefficient K_t for these three floaters have the same variation trends with wave

frequencies. Heave motion increases with the increase of D_2/D_3 ratio at low frequencies ω<3.8 rad/s, but decreases in the region of ω>4.3 rad/s. As shown in Fig. 23 (b), the peak value of the conversion efficiency moves towards lower frequency region with the increasing of D_2/D_3 due to the change of the mass of floaters. The maximum η_e reaches 80.0% when D_2/D_3=2.6723 at a frequency of ω=4.02 rad/s. Decreasing the D_2/D_3 ratio results in a small reduction in conversion efficiency, and a transition to peak efficiency at higher frequencies (ω=4.286 rad/s for D_2/D_3=1.3466). Increasing the ratio of D_2/D_3 reduces the transmission coefficient of the floater and improves the reflection coefficient of the floater in the region ω>4.1 rad/s. This is because the decrease of the ratio of baffle height D_2/D_3 leads to the inclination angle of the triangular part D_2 becoming smaller, resulting in the improvement of the wave attenuation and the wave reflection ability.

5. Conclusions

In this study, the hydrodynamic performance of floating breakwaters with different bottom shapes, which can also serve as an oscillating-buoy type wave energy converter (WEC), is investigated using the Star CCM+ CFD commercial package. The convergence study of mesh size and time step and comparison to higher order analytical solutions shows that waves generated by the present model are stable along the propagation direction and sufficiently accurate (within 3.5%). Comparisons with the published experimental results of Ning et al. [16] and Madhi et al. [24] show the present model can accurately predict the interaction between the waves and floaters with different shapes. The optimal damping b_{opt} can be calculated based on potential flow theory and agrees well with the present CFD results. The heave motion, wave energy conversion efficiency, reflection coefficient, transmission coefficient and dissipation coefficient of the integrated system with different bottom shapes, widths and drafts are investigated respectively. The conclusions are summarized as follows:

(1) Bottom shape can have a pronounced effect on the conversion efficiency and transmission coefficient of the integrated system, especially for long waves. The floater with square bottom has the lowest conversion efficiency and the largest transmission and reflection coefficients compared with other asymmetrical floaters. The hydrodynamic performance of a new floater with triangular-baffle bottom is comparable to that with Berkeley-Wedge bottom, which has a high conversion efficiency (near 90%) and strong wave elimination performance as verified by experiments of Madhi et al. [24]. The addition of the baffle greatly improves the hydrodynamic performance of the floater with triangular bottom in the low frequency region.

(2) The width, the ratio of D_1/D and the ratio of D_2/D_3 (where D, D_1, D_2, D_3 are the draft, the upper vertical side, the triangular part, the lower vertical baffle part of the floater, as shown in

Fig.16) of the floater have a significant influence on the conversion efficiency of the integrated system with triangular-baffle bottom. The influence of the floater width on the conversion efficiency and reflection coefficient is more significant for long waves, but the ratios of D_1/D and D_2/D_3 are more significant for short waves. However, the influence of the width on the transmission coefficient is minor, as the draft of the floaters is kept constant. The transmission coefficients of the floaters with different ratios of D_1/D or D_2/D_3 are almost the same for long waves but have noticeable differences for short waves. By optimizing the width, the ratio of D_1/D and D_2/D_3 of floater, it is possible to lower the transmission coefficient and achieve satisfactory conversion efficiency.

(3) The decrease of the upper vertical part D_1 can increase the energy conversion efficiency and maintain satisfactory wave attenuation performance. Furthermore, weaker vortices develop with the smaller upper vertical section, which leads to less energy dissipation.

(4) By carefully selecting parameters of the floater, it is possible to optimize wave energy conversion and attenuation performance of the WEC-type floating breakwater and broaden the effective frequency range.

This study has demonstrated the potential for cooperation between wave energy utilization and coastal protection. Wave energy converters with good energy extraction and coastal protect performance have been identified, and guidance for practical engineering design has been developed. The cost-sharing achieved through an integrated system may help make wave energy economically competitive.

Acknowledgement

This work was supported by the National Natural Science Foundation of China (51761135013, 51409066), the UK Engineering and Physical Sciences Research Council (EPSRC) through grant EP/R007497/1, the Natural Environment Research Council UK, the High-tech Ship Research Projects Sponsored by Ministry of Industry and Information Technology of the People's Republic of China-Floating Support Platform Project (the second stage) (MIIT201622), and the International Clean Energy Talent Program 2017 of China Scholarship Council.

This work was also supported by the Lloyd's Register Foundation (LRF) through the joint centre involving University College London, Shanghai Jiaotong University and Harbin Engineering University. The LRF helps to protect life and property by supporting engineering-related education, public engagement and the application of research.

References

[1] Falnes J. A review of wave energy extraction. Marine Struct 2007; 4: 185-201.

[2] Astariz S, Iglesias G. The economics of wave energy: A review. Renew Sustain Energy Rev 2015; 45:397-408.

[3] Mustapa MA, Yaakob OB, Ahmed YM. Wave energy device and breakwater integration: A review. Renew Sustain Energy Rev 2017; 77:43-58.

[4] Zhao XL, Ning DZ, Zou QP, Qiao DS, Cai SQ. Hybrid floating breakwater-WEC system: A review. Ocean Eng 2019; 186:106126.

[5] McCartney BL. Floating breakwater design. J Waterw Port, Coast Ocean Eng 1985;111(2): 304-318.

[6] Ji CY, Chen X, Cui J, Gaidai O, Incecik A. Experimental study on configuration optimization of floating breakwaters. Ocean Eng 2016; 117: 302–310.

[7] Dai J, Wang CM, Utsunomiya T. Review of recent research and developments on floating breakwaters. Ocean Eng 2018; 158:132-151.

[8] He F, Huang ZH, Law WK. An experimental study of a floating breakwater with asymmetric pneumatic chambers for wave energy extraction. Appl Energy 2013; 106(11): 222-231.

[9] He F, Leng J, Zhao XZ. An experimental investigation into the wave power extraction of a floating box-type breakwater with dual pneumatic chambers. Appl Ocean Res 2017; 67: 21-30.

[10] He F, Zhang HS, Zhao JJ, Zheng SM, Iglesias G. Hydrodynamic performance of a pile-supported OWC breakwater: An analytical study. Appl Ocean Res 2019; 88:326-340.

[11] Xu CH, Huang ZH. A dual-functional wave-power plant for wave-energy extraction and shore protection: A wave-flume study. Appl Energy 2018; 229: 963-976.

[12] Zheng SM, Zhang YL, Iglesias G. Coast/breakwater-integrated OWC: A theoretical model. Marine Struct 2019; 66:121-135.

[13] Giacomo M, Giovanni M, Andrea S, Luca D, Alessandra R, Rocco V, Marco F, Felice A. Modelling and field testing of a breakwater-integrated U-OWC wave energy converter with dielectric elastomer generator. Renew Energy 2020; 146: 628-642.

[14] Contestabile P, Iuppa C, Lauro ED, Cavallaro L, Andersen TL, Vicinanza D. Wave loadings acting on innovative rubble mound breakwater for overtopping wave energy conversion. Coast Eng 2017; 122: 60–74.

[15] Yueh CY, Chuang SH. A boundary element model for a partially piston-type porous wave energy converter in gravity waves. Eng Anal Bound. Elem 2012; 36: 658–664.

[16] Ning DZ, Zhao XL. Hydrodynamic performance of a pile-restrained WEC-type floating breakwater: An experimental study. Renew Energy 2016; 95: 531-541.

[17] Zhao XL, Ning DZ. Experimental investigation of breakwater-type WEC composed of both stationary

and floating pontoons. Energy 2018; 155:226-233.

[18] Zhao XL, Ning DZ, Liang DF. Experiment investigation on hydrodynamic performance of a breakwater-integrated WEC system. Ocean Eng 2019; 171:25-32.

[19] Zhao XL, Ning DZ, Zhang CW, Kang HG. Hydrodynamic Investigation of an Oscillating Buoy Wave Energy Converter Integrated into a Pile-Restrained Floating Breakwater. Energies 2017; 10:712.

[20] Ning DZ, Zhao XL, Zhao M, Hann M, Kang HG. Analytical investigation of hydrodynamic performance of a dual pontoon WEC-type breakwater. Appl Ocean Res 2017; 65:102-111.

[21] Jin S, Patton R. Geometry Influence on Hydrodynamic Response of a Heaving Point Absorber Wave Energy Converter. European Wave and Tidal Energy Conference; 2017.

[22] Chen Q, Zang J, Birchall J, Ning DZ, Zhao XL, Gao JL. On the hydrodynamic performance of a vertical pile-restrained WEC-WECtype floating breakwater. Renew Energy 2020; 146:414-425.

[23] Yeung RW, Wehausen JV, Webster WC. Hydrodynamics of ships and ocean systems-II, lectures notes for course NAOE-241b. Tech.rep., University of California at Berkeley; 1983.

[24] Madhi F, Sinclair ME, Yeung RW. The Berkeley Wedge: an asymmetrical Energy-Capturing floating breakwater of high performance. Marine Syst & Ocean Tech., 2014; 9(1): 05-16.

[25] Zhang WC, Liu HX, Zhang L, Zhang XW. Hydrodynamic analysis and shape optimization for vertical axisymmetric wave energy converters. China Ocean Eng 2016; 30: 954–966.

[26] Chen ZF, Zhou BZ, Zhang L, Zhang WC, Wang SQ, Zang J. Geometrical evaluation on the viscous effect of point-absorber wave-energy converters. China Ocean Eng 2018;32(4): 443-452.

[27] Reabroy R, Zheng XB, Zhang L, Zang J, Yuan Z, Liu MY, Sun K, Tiaple Y. Hydrodynamic response and power efficiency analysis of heaving wave energy converter integrated with breakwater. Energy Convers Manage 2019; 195: 1174-1186.

[28] Bilandi RN, Jamei S, Roshan F. Numerical simulation of vertical water impact of asymmetric wedges by using a finite volume method combined with a volume-of-fluid technique. Ocean Eng 2018; 160:119-131.

[29] Fábio MMM, António M G L, Almerindo D F. Numerical simulation of regular waves: Optimization of a numerical wave tank. Ocean Eng 2018; 170:89–99.

[30] Fenton JD. A fifth-order stokes theory for steady waves. J Waterw Port, Coast Ocean Eng 1985; 111(2): 216-234.

[31] Mojtaba MA, Paulo TE, Marcelo AV, Sergio HS. How does the free surface affect the hydrodynamics of a shallowly submerged submarine. Appl Ocean Res 2018; 76:34-50.

[32] Völkner S, Brunswig J, Rung T. Analysis of non-conservative interpolation techniques in overset grid finite-volume methods. Comput Fluids 2017; 148:39–55.

[33] Sun SY, Sun SL, Wu GX. Fully nonlinear time domain analysis for Hydrodynamic performance of an oscillating wave surge converter. China Ocean Eng 2018; 32(5): 582-592.

[34]Zhou BZ, Ning DZ, Teng B, Bai W. Numerical investigation of wave radiation by a vertical cylinder using a fully nonlinear HOBEM. Ocean Eng 2013; 70:1-13.

[35]Zhou BZ, Wu L, Xu GD. Resonance of the roll motion of a two dimensional barge induced by triple frequency wave force. Ocean Eng 2017; 134:13-23.

[36]Budar K, Falnes J. A resonant point absorber of ocean-wave power. Nat 1975;256 (5517) :478-479.

[37]Goda Y, Suzuki T. Estimation of incident and reflected waves in random wave experiments. In: Proc. of 15th Coastal Engineering Conference; Hawaii, 1976; 828-845.

[38]Yang ZY. Large-eddy simulation: Past, present and the future. Chin J Aeronaut 2015; 28(1): 11–24.

[39]Huai X, Joslin RD, Piomelli U. Large-Eddy Simulation of Transition to Turbulence in Boundary Layers. Theoret. Comput. Fluid Dynamics 1997; 9(2): 149–163.

[40]Piomelli U. Large-eddy simulation: achievements and challenges. Prog Aero Sci 1999; 35(4):335-362.

[41]Rienecker MM, Fenton JD. A Fourier approximation method for steady water waves. J. Fluid Mech 1981; 104:119-137.

[42]Westphalen J, Greaves DM, Williams CJK, Hunt-Raby AC, Zang J. Focused waves and wave-structure interaction in a numerical wave tank. Ocean Eng, 2012, 45(5):9-21.